MEASUREMENTS OF THE SPATIO-TEMPORAL PROFILES OF FEMTOSECOND LASER PULSES

A Thesis
Presented to
The Academic Faculty

by

Pablo Gabolde

In Partial Fulfillment
of the Requirements for the Degree
Doctor of Philosophy in the
School of Physics

Georgia Institute of Technology

August 2007

MEASUREMENTS OF THE SPATIO-TEMPORAL PROFILES OF FEMTOSECOND LASER PULSES

Approved by:

Dr. Rick Trebino, Advisor
School of Physics
Georgia Institute of Technology

Dr. T.A. Brian Kennedy
School of Physics
Georgia Institute of Technology

Dr. Alex Kuzmich
School of Physics
Georgia Institute of Technology

Dr. Jennifer Curtis
School of Physics
Georgia Institute of Technology

Dr. John A. Buck
School of Electrical and Computer Engineering
Georgia Institute of Technology

Date Approved: June 26, 2007

ACKNOWLEDGEMENTS

I would like to thank my advisor, Rick Trebino, for accepting me in his research group and for suggesting the project of completely measuring ultrashort pulses using digital holography. This original idea evolved into an entire thesis that covered many areas of ultrafast optics; it has been very rewarding to start such a project from scratch to finish with a working prototype (STRIPED FISH). Additionally, I would like to acknowledge the experience and skills of Mark Kimmel, our previous lab manager.

I received a lot of help from fellow graduate students (and post-docs) of the group. The list is long (Aparna, Dongjoo, Erik, Kristan, Lina, Neeraj, Pam, Qiang, Saman, Selcuk, Xuan, Xun, Zyiang) but I need to especially thank Xun for patiently answering many of the questions I had during my first years in the group. Also, several projects in the lab required a considerable amount of team work; it has been very pleasant to work with Dongjoo and Pam on some experiments, and with Wafa Amir as part of a collaboration with the group of Jeff Squier at the Colorado School of Mines.

Finally, I would like also to thank Linda Trebino for her constant assistance with administrative matters, and the members of the department staff (in particular from the financial, administrative, facility and IT offices) for their extraordinary patience and diligence.

TABLE OF CONTENTS

LIST OF TABLES

LIST OF FIGURES

LIST OF SYMBOLS AND ABBREVIATIONS

CPA ..... Chirped-pulse amplification

DOE ..... Diffractive optical element

GD ..... Group delay

GDD ..... Group-delay dispersion

FROG ..... Frequency-resolved optical gating

SI ..... Spectral interferometry

STRIPED FISH ..... Spatially and temporally resolved intensity and phase evaluation device: full information from a single hologram

SUMMARY

The main contributions of this thesis to the field of ultrashort pulse measurement are a new set of experimental tools to measure the spatio-temporal fields of femtosecond pulses, and a new simplified formalism to describe such fields in the presence of distortions.

More specifically, we developed an experimental technique based on scanning-wavelength digital holography and frequency-resolved optical gating that allows the complete measurement of the electric field $E(x,y,t)$ of trains of identical femtosecond pulses. A related method, wavelength-multiplexed digital holography, is also introduced. It achieves a *single-shot* measurement of the three-dimensional field $E(x,y,t)$ – but at a reduced resolution – using a simple experimental apparatus. Both methods can be used to measure various spatio-temporal distortions that often plague femtosecond laser systems, in particular amplified ones.

Finally, to unambiguously and intuitively quantify such distortions, we introduce normalized correlation coefficients so that a common language can be used to describe the severity of these effects.

CHAPTER 1

INTRODUCTION

1.1 Femtosecond laser pulses and their measurement

Laser pulses with durations in the femtosecond regime (1 fs = 10^{-15} s) are now routinely generated by extremely stable research and commercial systems in laboratories around the world. To date the most widespread femtosecond lasers are based on a titanium-doped sapphire (Ti:Al_2O_3) gain medium [1] and readily generate pulse energies of a few nanojoules with durations of a few tens of femtoseconds. Lasers with pulse durations that rival with one optical cycle (2.7 fs at 800 nm) are even commercially available [2]. Although their average power is usually moderate, these lasers – often called Ti:sapphire "oscillators" – readily reach *peak* powers of hundreds of kilowatts and intensities on the order of 10^{13} W/cm^2 when they are focused, resulting in many materials in a nonlinear response to the incident optical field. Such nonlinear optical effects result in a wide range of easily observed phenomena, from harmonics generation [3] to optical mixing [4] to multi-photon fluorescence [5]. An even wider range of nonlinear optical processes can be observed if an amplified laser chain follows a Ti:sapphire oscillator to yield energies of a few millijoules and above, and intensities in excess of 10^{21} W/cm^2 [6].

The development of such lasers with ever shorter pulse durations, higher pulse energy, and improved beam quality has naturally sustained the need for improved pulse measurement techniques over the last few decades. Of all these measurement, the

characterization of the pulse temporal shape is certainly the most delicate, because of the time scales involved, which are several orders of magnitude below the response time of optoelectronic components such as photo-diodes. Consequently, most techniques rely on the fast nonlinear optical response of specific materials, in particular optical crystals, to achieve the required femtosecond time resolution. For instance, a common way to estimate the pulse duration of femtosecond pulses is to record the intensity auto-correlation at the second harmonic in a doubling crystal, using a delay line to scan (in space) the relative delay between a pulse and its replica, while an slow detector records the time-integrated second-harmonic signal [7]. Unfortunately, such an approach only yields partial information about the pulse under test, but more elaborate techniques are available to fully characterize (i.e., in intensity and phase) the temporal electric field, $E(t)$.

These techniques, in particular frequency-resolved optical gating (FROG) [8], can additionally provide some *spatial* information about the electric field [9]. However, they fall short of providing a complete characterization of the electric field representing an ultrashort laser pulse, $E(x,y,t)$.

In this study, we present experimental and mathematical techniques that enable the complete characterization of the electric field, $E(x,y,t)$, and its departures from an ideal profile. This information proves to be invaluable to optimize the performance of amplified systems, often plagued by spatio-temporal distortions of the field, and could also open the way to the development of new diagnostic tools providing time-resolved information of samples with a complex spatial structure.

1.1.1 Femtosecond pulse generation

Modern femtosecond lasers often generate trains of femtosecond pulses by passive "mode-locking": a passive element is introduced in the laser cavity to favor the operation of the laser in a pulsed mode rather than in a continuous-wave (c.w.) operation. Common elements include a saturable absorber (usually a dye [10] or a semi-conductor [11]) or an aperture used in conjunction with the optical Kerr effect [12, 13]. Such elements are placed within a dispersion-compensated laser cavity that can support a large lasing bandwidth.

In this study we have mostly used femtosecond oscillators (KMLabs Inc.) based on Ti:sapphire (Ti:Al_2O_3) as the gain medium. Ti:sapphire benefits from a very good thermal conductivity, a large emission bandwidth covering 650 to 1100 nm [1], and an absorption spectral region that conveniently contains 532 nm, a wavelength easily and efficiently accessed by optical pumping with a frequency-doubled neodymium vanadate (Nd:YVO_4) solid-state laser (Coherent Verdi). Passive mode-locking is achieved by Kerr lensing with a "soft" aperture. In the mode-locked operation, pulses self-focus in the Ti:sapphire crystal and their mode is matched to the pump laser mode, while in the c.w. operation the laser beam does not self-focus, resulting in a mode mismatch with the pump beam (and therefore in a reduced gain). Mode-locking is not self starting but is obtained by a mechanical perturbation of the cavity. Intra-cavity dispersion compensation is achieved by a pair of prisms arranged to form a Treacy pulse compressor [14], although more recently dielectric mirrors featuring negative dispersion have gained in popularity [15]. The linear cavity is folded to compensate for astigmatism [16]. With an optical

pump power of 5 W, we routinely obtain pulses at the nJ level with ~35 nm of bandwidth (FWHM) and a repetition rate set by the cavity length at 89 MHz.

Experiments requiring higher pulse energies were performed using a chirped-pulse amplification (CPA) [17] system (Quantronix RGA 4800). The peak power of the pulses from the Ti:sapphire oscillator is first decreased by a grating stretcher before these seed pulses are injected at 1 kHz and safely amplified to ~300 μJ in a regenerative Ti:sapphire laser. The amplified pulses are finally recompressed to ~150 fs by a grating compressor.

1.1.2 Applications of femtosecond laser pulses

Femtosecond laser pulses have a wide range of applications because they easily allow access to very high intensities, and therefore to nonlinear light–matter interactions. Uses of these lasers abound, ranging from micro-machining [18] to bio-medical imaging [5] to spectroscopy [19] and coherent control [20]. In many of these applications, the shortest possible pulse must be delivered to the smallest possible area, in order to deliver the highest intensity onto a sample. In other words, the focused pulse should ideally reach *both* its transform limit and its diffraction limit on the focal plane. This requires an optimal spatio-temporal profile free of spatio-temporal distortions. It is only by experimentally measuring the complete spatio-temporal profile of pulses that their spatio-temporal quality can be quantified and monitored as adjustments are made to the laser system.

1.1.3 Standard measurement techniques and their limits

To achieve temporal resolution on the femtosecond regime, most measurement techniques rely on fast nonlinearities to generate optical signals that are then measured by slow (time-averaging) detectors such as photo-diodes or digital sensors (e.g., charge-coupled devices or complementary metal–oxide–semiconductor imagers). A simple but commonly used technique is the intensity autocorrelation [21]. A pulse with amplitude $E(t)$ and intensity $I(t)$ and a replica delayed by a time τ are mixed in a doubling crystal to produce an optical field that is proportional to $E(t)E(t-\tau)$. This field has a frequency that corresponds to the second harmonic of the pulse under test, and an intensity that is proportional to $I(t)I(t-\tau)$. The signal recorded by a slow detector such as a photo-diode is then

$$A(\tau) = \int_{-\infty}^{+\infty} I(t)I(t-\tau)dt \tag{1.1}$$

and corresponds to the intensity autocorrelation of the pulse under test as a function of delay τ. By varying τ using a delay line, one can record the function $A(\tau)$ whose width can be related to the width of the intensity $I(t)$, *assuming* that the shape (Gaussian, sech^2, etc…) of $I(t)$ is known (see Appendix A for more details).

Most of the time, however, the temporal shape of the pulse is precisely the information that is sought. In that case, one can measure the spectrum of the second harmonic generated at each delay τ to reconstruct a two-dimensional signature (in the time-frequency domain) of the pulse under test. This "signature" of the pulse in the time-frequency domain contains enough information to essentially retrieve the electric field of

the pulse under test. This technique is called second-harmonic frequency-resolved optical gating (FROG) and can be adapted to various pulse measurement situations by choosing a suitable beam geometry and nonlinear medium [22]. It is presented in more details in Appendix A.

However, the FROG technique and other femtosecond pulse measurement techniques are often restricted to a temporal measurement of the pulse, and only provide limited – if any – information regarding the spatial dependence of the pulse. As a result, researchers frequently measure the spatial profile of the laser beam independently from its temporal profile. The spatial intensity can be imaged onto a digital camera, while the spatial wave-front can be measured by a Shack-Hartmann sensor [23, 24] or by shearing interferometry [25, 26]. These spatial measurements, however, are usually averaged over the bandwidth (or, equivalently, the duration) of the pulse under test. As such, they do not constitute a complete measurement of the electric field of the pulse under test, in particular when spatio-temporal distortions are present [27]. Now that femtosecond lasers are reaching their fundamental limit in terms of pulse duration (one optical cycle), there is an increasing interest in the study of such distortions, and in their measurement.

1.2 Thesis outline

This thesis describes experimental techniques that have been developed to measure the spatio-temporal profile of femtosecond laser pulses. Two seemingly opposite goals are stressed: the measurement of “clean” pulses delivered by a well-aligned laser system and the measurement of complicated pulses resulting from a voluntary shaping of the pulse or from an interaction with a medium for diagnostic purposes. Both aims

require a common device, one that allows for the measurement of the spatio-temporal electric field of the pulses under test.

Chapter 2 reviews methods based on spectral interferometry that allow one- and two-dimensional measurements of the electric field, $E(t)$ or $E(x,t)$. Spectral interferometry is well-suited to the measurement of optical distortions introduced by elements possessing a cylindrical symmetry, such as high-numerical-aperture microscope objectives, and allows the measurement of temporal pulse shapes with a high spectral resolution. The principles of spectral interferometry are reviewed, and its experimental implementation is presented in several situations.

Chapter 3 extends the interferometric method of Chapter 2 to systems lacking cylindrical symmetry (such as amplified laser systems containing grating stretchers and compressors) and presents a new method that combines digital holography and FROG. Using a wavelength scan, it allows the measurement of the complete spatio-temporal electric field, $E(x,y,t)$, of trains of identical pulses.

Chapter 4 further extends this wavelength-scan method to the measurement of *single* laser shots by using a geometry containing a diffractive optical element (DOE) to perform a complete three-dimensional measurement of $E(x,y,t)$ using a single two-dimensional camera frame.

Chapter 5 introduces a new formalism to describe spatio-temporal distortions in femtosecond laser pulses that is both consistent with previous approaches and emphasizes the severity of these distortions. This formalism is based on normalized correlation coefficients. Such parameters are well-suited to the study of slightly-misaligned optical systems, and provide an intuitive feedback to the user in the laboratory.

Finally, Appendix A provides a short overview of FROG, the technique that is used in many of the experiments presented in this study to measure the temporal profile of an undistorted reference pulse.

CHAPTER 2

INTERFEROMETRIC MEASUREMENTS OF FEMTOSECOND PULSES

Portions of the work presented in this chapter originally appeared in the following papers: [28] W. Amir, T.A. Planchon, C.G. Durfee, J.A. Squier, P. Gabolde, R. Trebino and M. Müller, *Simultaneous visualization of spatial and chromatic aberrations by 2D Fourier Transform Spectral Interferometry*, Optics Letters **31** (19) 2927-2929 (2006); and [29] P. Bowlan, P. Gabolde, A. Shreenath, K. McGresham, S. Akturk and R. Trebino, *Crossed-beam spectral interferometry: a simple, high-spectral-resolution method for completely characterizing complex ultrashort pulses in real time*, Optics Express **14** (24) 11892-11900 (2006).

2.1 Intensity-and-phase interferometric measurements

Interferometric techniques are often used in ultrafast optics because they allow the determination of phase quantities from an intensity measurement. These phase functions can depend on numerous physical variables, such as angular frequency ω, time t, position x and spatial frequency k_x.

Mathematically, an interference pattern I of two fields E_1 and E_2 written as a function of a generic variable v is of the form

$$\begin{aligned} I(v) &= \left|E_1(v) + E_2(v)\right|^2 \\ &= \left|E_1(v)\right|^2 + \left|E_2(v)\right|^2 + 2\left|E_1(v)\right|\left|E_2(v)\right|\cos\left(\varphi_1(v) - \varphi_2(v)\right) \end{aligned} \tag{2.1}$$

The last term of Equation (2.1) depends of the phase difference of the two interfering fields. Various schemes, such as phase stepping [30, 31] or fringe demodulation [32], may be used to numerically extract that phase difference $\varphi_1(v) - \varphi_2(v)$ from a measured interferogram $I(v)$, allowing the determination of φ_1 if φ_2 is known. The

choice of E_2 (and thereby of φ_2) is therefore capital. In some cases, it must correspond to a pre-characterized reference pulse. In other cases, it is possible to construct E_2 from E_1 to obtain a self-referenced method such as shearing interferometry [25] (see Section 3.3). In either case, $|E_1(\nu)|^2$ can also be numerically extracted from $I(\nu)$ so that a complete intensity-and-phase characterization of E_1 is possible.

2.2 One-dimensional interferometric measurement of $E(t)$

Spectral interferometry consists of recording an interferogram of two pulses in the spectral domain, i.e., $\nu = \omega$ in Equation (2.1). Typically, an unknown signal pulse, $E_1(\omega) = E_s(\omega)$, interferes in a spectrometer with a reference pulse delayed by an amount τ, $E_2(\omega) = E_r(\omega)\exp(-i\tau\omega)$. The delay τ generates spectral fringes whose shape encodes the spectral phase difference of the two pulses. An algorithm based on Fourier transforms is then used to extract the phase of the signal pulse, $\varphi_s(\omega)$, from the spectral interferogram [33]. The spectral interferogram $I(\omega)$ is simply given by:

$$\begin{aligned} I(\omega) &= \left|E_s(\omega) + E_r(\omega)\right|^2 \\ &= \left|E_s(\omega)\right|^2 + \left|E_r(\omega)\right|^2 + 2\left|E_s(\omega)\right|\left|E_r(\omega)\right|\cos\left(\varphi_r(\omega) - \varphi_s(\omega) + \tau\omega\right) \end{aligned} \tag{2.2}$$

Application of the algorithm yields the intensity, $|E_s(\omega)|^2$, and phase, $\varphi_s(\omega)$, of the unknown signal pulse if similar quantities are known for the reference pulse. (A

description of the algorithm is provided in Section 3.1.3.) This permits a one-dimensional characterization of the field of the unknown pulse, $E(\omega)$, or of its Fourier transform, $E(t)$.[†]

A modified version of spectral interferometry uses sum-frequency generation with a chirped pulse to produce the second field, $E_2(\omega)$, from the unknown pulse $E_1(\omega) = E(\omega)$. The resulting field is a frequency-sheared time-delayed replica of $E(\omega)$: $E_2(\omega) = E(\omega - \delta\omega)\exp(-i\tau\omega)$ [34]. In this case, the phase difference that is reconstructed by the algorithm is approximately equal to $\delta\omega\, \varphi'(\omega)$, where $\varphi(\omega)$ is the spectral phase of the unknown pulse. The spectral phase is then readily calculated by direct integration. The spectral intensity, $|E(\omega)|^2$, is measured separately to complete the self-referenced one-dimensional interferometric characterization of $E(\omega)$, and thus of $E(t)$.

2.3 Two-dimensional interferometric measurement of $E(x,t)$

The interferogram of Equation (2.2) can additionally be spatially resolved and recorded using a two-dimensional digital camera to yield the interferogram $I(x,\omega)$:

$$\begin{aligned} I(x,\omega) &= \left|E_s(x,\omega) + E_r(x,\omega)\right|^2 \\ &= \left|E_s(x,\omega)\right|^2 + \left|E_r(x,\omega)\right|^2 \\ &\quad + 2\left|E_s(x,\omega)\right|\left|E_r(x,\omega)\right|\cos\left(\varphi_r(x,\omega) - \varphi_s(x,\omega) + \tau\omega\right) \end{aligned} \tag{2.3}$$

Experimentally this is achieved by imaging the x-coordinate of the laser beam onto the slit of an imaging spectrometer. Note that although interference fringes are

---

[†] To simplify notations and avoid symbols such as $\tilde{E}, \hat{\tilde{E}}$, etc…, functions that are Fourier transform pairs are simply distinguished by their argument, e.g., $E(\omega)$ and $E(t)$; $E(x)$ and $E(k_x)$; $I(x,\omega)$ and $I(x,t)$.

created along the frequency axis ω, the shape of these fringes also depends on the *spatial* dependence of the phase. Therefore, the standard Fourier transform algorithm yields not only the spectral dependence of the phase of the signal pulse, but also its spatial dependence, along with possible spatio-spectral couplings, because the phase function $\varphi_s(x,\omega)$ is completely characterized. This is especially useful to determine pulse distortions that are introduced by optical components that would be unaccounted for if independent spatial and spectral measurements had been performed.

2.3.1 Motivations for measuring $E(x,t)$

Many applications involving femtosecond pulses, such as multi-photon microscopy or micro-machining, require a precise control over the electric field of the pulses. Improved resolution is attained when the pulses are focused to the smallest "volume" $\sim\lambda^3$, the product of a diffraction-limited area ($\sim\lambda^2$) by the spatial extent of one optical cycle ($\sim\lambda$). Achieving this limit requires the use of multi-element focusing optics that unfortunately often introduce distortions. The first drawback of these optical elements is that they lengthen pulses due to material dispersion. When this dispersion is uniform across the whole beam, it can be compensated by a Treacy pulse compressor [35], but for imaging systems used in microscopy, dispersion effects can also introduce radially-dependent pulse shapes that are more difficult to compensate for. Additional geometrical aberrations also affect the pulse profile. Such effects are much more difficult to correct, or even to characterize, and in practice such optical systems are simply aligned for maximum efficiency of a particular signal (for example, two-photon fluorescence). The design of higher-performance systems, however, would greatly benefit from a more

thorough investigation of the distortions introduced by its optical components. Because of the cylindrical symmetry of these systems, only the measurement of the electric field $E(r,t)$ (or $E(r,\omega)$) is required.

2.3.2 Geometrical and chromatic aberrations of the pulse-front

Distortions to the pulse-front due to focusing optics can generally be traced to two sources: geometrical aberrations, and dispersive effects. Geometrical aberrations, such as defocus, astigmatism, coma, or spherical aberrations, lead primarily to distortions of the wave-front. Dispersive effects on the other hand usually result in a position-dependent delay between the wave-front and the pulse-front. Thus in general, geometrical and dispersive (or "chromatic") aberrations both result in distortions to the pulse-front, albeit for different reasons.

We first unambiguously define the pulse-front: it is simply the energy front of the pulse. Roughly speaking, it is the time of arrival of the pulse at a given position x, $t_0(x)$. More formally, it is the position-dependent first-order temporal moment of the pulse intensity, $|E(x,t)|^2$:

$$t_0(x) = \frac{\int_{-\infty}^{+\infty} t\left|E(x,t)\right|^2 dt}{\int_{-\infty}^{+\infty} \left|E(x,t)\right|^2 dt} \tag{2.4}$$

Ideally, the pulse-front of a collimated beam should be constant (in space), and the pulse-front of a focused pulse should be spherical. More generally, the laser beam should have an ideal wave-front to allow for a diffraction-limited profile for a particular

application, and the pulse-front should match that function (up to an additive constant independent of x).

A common geometrical aberration that prevents this situation is spherical aberration, which is present in singlet lenses whose surfaces are spherical, and to a lesser extend in doublets and triplets. It is calculated by expanding ray angles to the third order ($\sin\theta \simeq \theta - \theta^3/6$) [36]. Thus, it is one of the so-called third-order (or Seidel) aberrations, and is characterized by a fourth-order term in the pupil radius r. Seidel aberrations are usually calculated by ray tracing programs, but are inconvenient to use in the context of wave-front analysis by interferometric means because the set of Seidel aberration functions are not orthogonal. Instead, Zernike polynomials are preferred because of their orthogonality, and the fact that they clearly separate the radial and azimuthal coordinates r and φ [37]. Conversion from one set of parameters to the other is a linear algebra problem [38, 39]. It is important to note that *to first order*, such geometrical aberrations are independent of the wavelength.

Geometrical aberrations cause distortions to the wave-front, thereby distorting the pulse-front as well. The spherical Seidel aberration, for example, results in a wave-front (and thus also in a pulse-front) containing terms in x^4. It can be calculated explicitly in the case of plano-convex lenses by evaluating wave-front contributions beyond the second order [40, 41]:

$$\varphi_{sph}(x,\omega) = k\,\frac{n_0{}^2(n_0{}^2-4)+2n_0+4}{8n_0(n_0-1)^2(n_0+2)}\left(\frac{x}{f_0}\right)^3 x \qquad (2.5)$$

Note that spherical aberrations have the same sign as the focal length f_0: a negative lens can partially compensate the spherical aberrations introduced by a positive lens.

In addition to geometrical aberrations, the pulse-front is also affected by chromatic (i.e., dispersive) effects. In a lens, for example, chromatic aberrations can be interpreted as a wavelength-dependent focal length $f(\lambda)$. For instance, for a thin lens with radii of curvatures $R_{1,2}$, the focal length is given by [36]:

$$\frac{1}{f(\lambda)} = \left(n(\lambda) - 1\right)\left(\frac{1}{R_1} - \frac{1}{R_2}\right) \tag{2.6}$$

Because of the shape of the refractive index curve of typical glasses, longer wavelengths tend to have longer focal lengths. This frequency-domain picture translates in the time domain to a delay between the pulse-front and the wave-front [42]. As in any dispersive material, the pulse-front lags the wave-front, but in the case of chromatic aberrations in a lens, this lag is *position-dependent*. It is given by $\Delta t(x) = T_{chr}\, x^2$ [41, 42], where

$$T_{chr} = \frac{1}{2c(n_0 - 1) f(\lambda_0)} \lambda_0 \frac{dn}{d\lambda}. \tag{2.7}$$

This delay results in a pulse-front with a term $T_{chr}\, x^2$ that adds to the distortions of the wave-front. Note that this term is of the same order as a defocus term; in some situations defocus and chromatic aberrations can compensate each other and result in a flat pulse-front in a diverging beam [42]. In general, however, the detrimental effects of geometrical distortions add to the ones of chromatic aberrations. This is in particular true

in the case of simultaneous spherical and chromatic aberrations, a common situation in ultrafast optics [41].

2.3.3 Calculation of the pulse-front distortions from the phase $\varphi(x,\omega)$

As stated by Equation (2.4), the pulse-front $t_0(x)$ is defined from the spatially-resolved pulse intensity, $|E(x,t)|^2$. Unfortunately, directly measuring this quantity is not a simple task. Techniques that are commonly used to estimate the pulse temporal intensity, such as two-photon absorption autocorrelation [43, 44], integrate the beam intensity over its spatial profile. Spatially-resolved techniques that rely on a ring-shaped obstruction of the beam, for example autocorrelation in a doubling crystal [40, 45] or two-photon absorption current generation [46, 47], only yield a rough estimate of the pulse-front.

Fortunately, much more precise measurements of the pulse-front can be obtained by an interferometric measurement of the electric field in the spectral domain, because the spectral phase contains precious *temporal* information. Indeed, the spectral phase derivative (that may depend on position x) has units of time, and is called the group delay:

$$t_g(x,\omega) = \frac{\partial \varphi}{\partial \omega}(x,\omega) \tag{2.8}$$

Note that the group delay is a function of ω. Conveniently, the average of the group delay, weighed by the spectrum $|E(\omega)|^2$, is the mean time of a pulse [48]. This result is particularly useful because it rigorously connects the pulse-front (defined in the time domain) to the spectral phase (measured in the frequency domain):

$$t_0(x) = \frac{\int \frac{\partial \varphi}{\partial \omega}(x,\omega)\left|E(x,\omega)\right|^2 d\omega}{\int \left|E(x,\omega)\right|^2 d\omega} \tag{2.9}$$

Quite often the average of the group delay can be approximated by the group delay at the central frequency ω_0; in practice, the following calculation is used:

$$t_0(x) \simeq \frac{\partial \varphi}{\partial \omega}(x,\omega_0) \tag{2.10}$$

Therefore, distortions to the pulse-front can be calculated directly from the phase $\varphi(x,\omega)$. Furthermore, the contributions from geometrical aberrations and chromatic aberrations can be clearly isolated:

$$t_0(x) = \underbrace{\frac{\varphi(x,\omega_0)}{\omega_0}}_{\text{geometrical aberrations}} + \underbrace{\frac{\partial \varphi}{\partial \omega}(x,\omega_0) - \frac{\varphi(x,\omega_0)}{\omega_0}}_{\text{dispersive aberrations}} \tag{2.11}$$

Such an approach is useful for instance to distinguish which terms of order x^2 in the group delay $t_0(x)$ might come from defocus (a geometrical aberration) and from chromatic aberration (a dispersive effect).

By experimentally measuring the spatio-spectral phase, $\varphi(x,\omega)$, we can therefore measure spatial distortions to the pulse-front. An approximation that is commonly performed is to represent the aberrated pulse-front by a polynomial of the fourth order that is free of off-axis aberrations such as coma and astigmatism [40, 41]:

$$t_0\left(x\right) = T_{def}x^2 + T_{sph}x^4 - T_{chr}x^2 \tag{2.12}$$

In Equation (2.12), the first term originates from defocus, the second from spherical aberrations, and the third from chromatic aberrations. The parameters T_{def} and T_{chr} have units of fs/mm^2 and are characteristic of a lens system at a given wavelength; T_{sph}, in fs/mm^4, is also an intrinsic characteristic of a lens system. For a positive lens, T_{def} is negative before the focus, and positive after the focus, while T_{sph} and T_{chr} are positive and do not change sign through the focus.

The defocus term can be eliminated by properly aligning the lens system (e.g., a telescopic system such that $T_{def} \simeq 0$). However, chromatic and spherical aberrations are more difficult to compensate and require a particular care in designing the lenses (achromatic doublets and triplets, aspheric surfaces, apochromatic lenses). Based on the input pulse duration and lenses characteristics, it is possible to estimate which one of the spherical or chromatic aberrations will dominate [41].

2.3.4 Single-shot interferometric measurement of $\varphi(x,\omega)$

Spectral interferometry yields a single-shot measurement of $E(t)$ by interference with a pre-characterized reference pulse, and may be directly extended to one spatial dimension by imaging the dimension x of the laser beam along the slit of an imaging spectrometer [46, 49]. A common experimental setup is a standard Michelson interferometer followed by an imaging spectrometer, where the optical element under test is placed in the sample arm. When both pulses interfere, a two-dimensional spectral interferogram is obtained and analyzed by a standard Fourier transform method [30]: the Fourier transform of Equation (2.3) is taken along the frequency dimension to yield

$$
\begin{aligned}
I(x,t) &= \mathcal{F}\left[I(x,\omega)\right] \\
&= \mathcal{F}\left[\left|E_s(x,\omega)\right|^2 + \left|E_r(x,\omega)\right|^2\right] \\
&+ \mathcal{F}\left[E_s(x,\omega)E_r(x,\omega)^*\right] \otimes \delta_{-\tau}(t) \\
&+ \mathcal{F}\left[E_s(x,\omega)^* E_r(x,\omega)\right] \otimes \delta_{+\tau}(t)
\end{aligned}
\tag{2.13}
$$

Equation (2.13) is a direct application of the shift theorem, and results in three well-separated functions in the time domain, provided that the delay τ is much larger than the durations of the pulses of interest. By applying a (digital) band-pass filter centered at $t = +\tau$ followed by an inverse Fourier transform to Equation (2.13), the complex product $E_s(x,\omega)^*E_r(x,\omega)$ can be recovered, or "reconstructed". When the reference pulse $E_r(x,\omega)$ is fully characterized, $E_s(x,\omega)$ can be obtained by a simple division, and its phase $\varphi_s(x,\omega)$ is thus unambiguously known (i.e., modulo 2π). The complete reconstruction process is very fast since it is based on two fast Fourier transforms (FFT) and very robust since the phase information is encoded in the shape of the interference fringes. It is therefore largely immune to intensity distortions (noise, stray light, grating/detector spectral response) in the recorded image. Interferometric stability is not required since this method is based on a single laser-shot geometry, although an enhanced fringe visibility (obtained through shorter camera exposure times) results in an increased signal-to-noise ratio in the reconstructed phase $\varphi_s(x,\omega)$.

Once the spatio-spectral phase is digitally reconstructed, curve fitting is used to extract the parameters corresponding to defocus (T_{def}), spherical aberrations (T_{sph}), and chromatic aberrations (T_{chr}). To first order, T_{def} and T_{sph} only depend on ω_0, the central frequency of the spectrum, and are computed by curve fitting the phase delay $t_\varphi(x) = \varphi(x,\omega_0)/\omega_0$ to $T_{def}x^2 + T_{sph}x^4$. The chromatic aberration parameter T_{chr} is then

calculated by subtracting the phase delay $t_\varphi(x)$ from the pulse-front $t_0(x) = (\partial\varphi/\partial\omega)(x,\omega_0)$ and fitting the resulting function to $-T_{chr}\,x^2$.

2.3.5 Experimental results

Several focusing elements have been analyzed by using two-dimensional spectral interferometry. To facilitate the experiment, collimated beams are obtained by placing a mirror in the focal region of the optics under test to retro-reflect the light. This approximately doubles the amount of aberrations. Focusing elements suffering from aberrations do not have a clearly defined focal plane, since different wavelengths and radial positions focus at different axial positions. Measurements are therefore performed at the paraxial focal plane of the central wavelength, and at the "best focus" plane, i.e. where the spot size is the smallest.

Recorded interferograms are analyzed by the Fourier transform method, and the spatio-spectral phase is reconstructed (Figure 2.1). The various aberration parameters are obtained by the curve fitting method (Figure 2.2), with an estimated accuracy of ±3%. Results are summarized in Table 2.1. As can be seen, the measured aberrations are quite small, and in general for multi-photon microscopy, it is found that for pulses longer than 50 fs, aberrations are negligible [28].

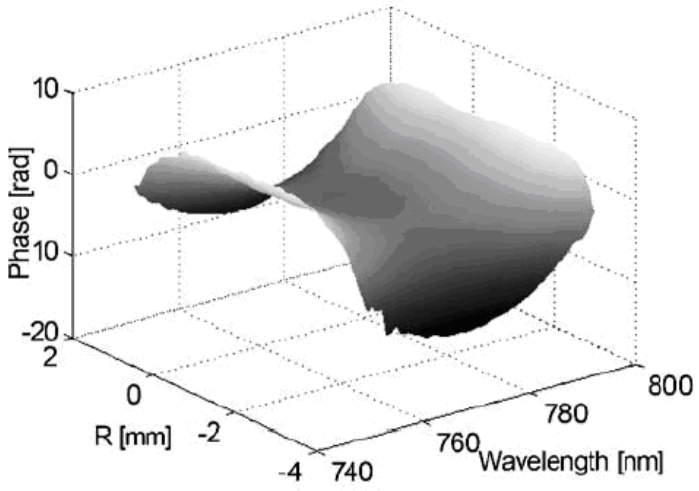

Figure 2.1. Spatio-spectral phase $\varphi_s(x,\omega)$ of an oil-immersion microscope objective reconstructed by two-dimensional spectral interferometry (published in Ref. [28]).

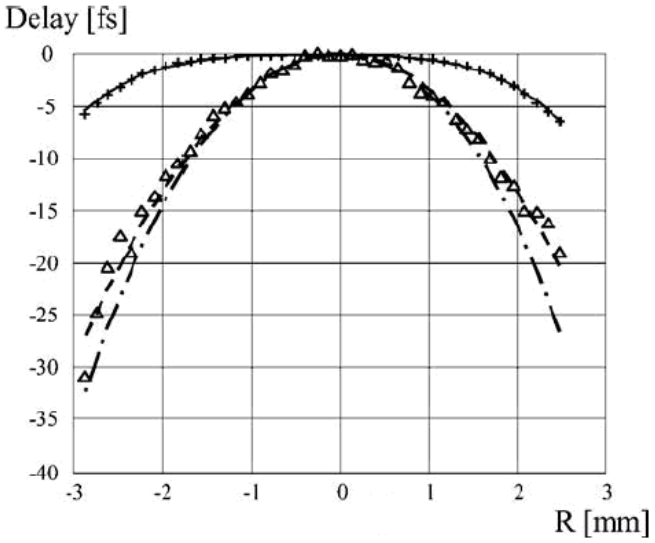

Figure 2.2. Curve fits to extract the parameters for defocus and spherical aberration (crosses), and chromatic aberration (triangles). The dashed line is the pulse-front. (Published in Ref. [28]).

Table 2.1. Measured aberration parameters in different optical systems (adapted from [28]).

Optical system	T_{def} [fs/mm^2]	T_{sph} [fs/mm^4]	T_{chr} [fs/mm^2]
Parabolic mirror (f = 12 mm)			
Paraxial focus	−	<0.001	0.36
Best focus	−	−0.008	0.35
Aspheric lens (New Focus, 20×, NA 0.50)	0.03	0.004	4.6
Microscope objective (Zeiss, 100×, NA 1.25)			
Paraxial focus	0.18	0.06	4.0
Best focus	−0.68	0.07	4.4

2.3.6 Spectral interferometry at zero delay

Spectral interferometry is usually performed by introducing a delay τ between the unknown signal pulse and the reference pulse in order to obtain the interference fringes as a function of frequency ω, as in Equation (2.3). Note that in this case position x and frequency ω play symmetric roles, except for the presence of the term $\omega\tau$ in the cosine. The equivalent of this term in the spatial domain (i.e., $k_x x$) corresponds experimentally to crossing the signal and reference beams at an angle α, in which case the resulting interferogram becomes:

$$\begin{aligned} I(x,\omega) &= \left|E_s(x,\omega) + E_r(x,\omega)\right|^2 \\ &= \left|E_s(x,\omega)\right|^2 + \left|E_r(x,\omega)\right|^2 \\ &\quad +2\left|E_s(x,\omega)\right|\left|E_r(x,\omega)\right|\cos\left(\varphi_r(x,\omega) - \varphi_s(x,\omega) + (\omega/c)x\sin\alpha\right) \end{aligned} \tag{2.14}$$

In the small bandwidth approximation, the spatial period of the resulting fringes is constant and equal to $\lambda_0/\sin\alpha$, and spatial fringes are observed along the x dimension. The Fourier transform algorithm can still be used to reconstruct the spatio-spectral phase, $\varphi_s(x,\omega)$. At first sight, the interferogram of Equation (2.3) or the one of Equation (2.14) seem to yield the same information, i.e., $\varphi_s(x,\omega)$. However, when a relative delay τ is

used, Fourier filtering is performed in the spectral domain, resulting in a reduced *spectral* resolution in the reconstructed phase. When a small crossing angle is used, the phase is reconstructed with a reduced *spatial* resolution, while maintaining the full spectral resolution of the spectrometer that is used to perform the measurement [50].

To choose between crossing the reference and signal pulses, and introducing a relative delay, one must consider the complexity of the spatio-spectral field that is measured. When the electric field of the unknown pulse contains higher order terms in x than in ω, it is preferable to sacrifice spectral resolution. However, for pulses with a complicated spectral structure (and less or little spatial structure), it is preferable to generate spatial rather than spectral fringes, so that the spectral intensity and phase can be measured with the full spectral resolution of the imaging spectrometer.

Figure 2.3 illustrate this point. We show the result of the measurement of a pulse with a complex spectral structure that is performed with spectral interferometry at zero delay. The figure corresponds to a double pulse, with an inter-pulse separation of 14 ps. The spectrum and spectral phase of the double pulse contain very fine structures that are easily resolved by this measurement technique [29].

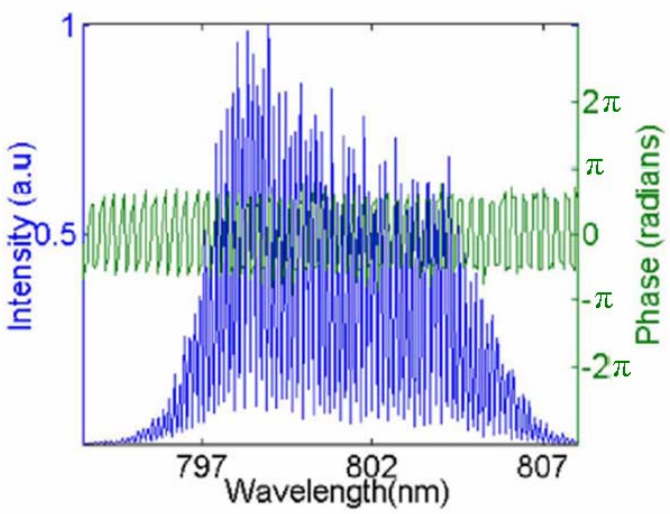

Figure 2.3. The reconstructed spectral electric field of a 14-ps double pulse generated using a Michelson interferometer (adapted from Ref. [29]).

2.4 Conclusions

Two-dimensional interferometric techniques such as spatially-resolved spectral interferometry are invaluable to measure either pulses with fine spectral features, or to measure in a single-shot geometry the two-dimensional electric field $E(x,\omega)$ or $E(x,t)$, provided that a reference pulse is available. As such, they are well suited to measure the distortions (or deliberate shaping) of pulses in two dimensions, in particular in optical systems that possess cylindrical symmetry. They can precisely measure distortions to the wave-front and pulse-front along one spatial coordinate x.

However, these techniques are not directly applicable to situations where the two spatial coordinates x and y play asymmetric roles. In the context of femtosecond lasers, this happens frequently: astigmatism in crystals cut at Brewster's angle or in off-axis curved mirrors [16], residual horizontal angular dispersion in prism and grating pulse

compressors [51], and various other distortions result in laser pulses with different characteristics along x and y, and in particular different spatio-temporal couplings along the horizontal and vertical dimensions.

In the next chapter, we introduce a new three-dimensional interferometric technique that characterizes the electric field of femtosecond pulses along *both* transverse spatial coordinates, allowing a complete characterization of the electric field at a given plane, $E(x,y,t)$.

CHAPTER 3

WAVELENGTH-SCANNING DIGITAL HOLOGRAPHY

The work presented in this chapter originally appeared in the following paper: [52] P. Gabolde and R. Trebino, *Self-referenced measurement of the complete electric field of ultrashort pulses*, Optics Express **12** (9) 4423-4429 (2004).

3.1 Digital holography

Digital holography is a spatial interferometric technique that is widely used to characterize light fields in intensity and phase, in particular if they are monochromatic. Traditionally, digital holography has been used in laser measurement to characterize the complex spatial electric field $E(x,y)$ of a single-frequency beam, but we will show in this chapter that this method can be extended to broadband light (such as femtosecond pulses). Used in combination with FROG, it can be applied to the measurement of the complete three-dimensional field of femtosecond pulses, $E(x,y,t)$.

3.1.1 Comparison with film-based holography

In holography, an interference pattern is recorded as a function of one or two spatial coordinates. The traditional recording media (photographic films) have been replaced by photo-detectors such as digital cameras that have opened the field of *digital* holography, where data acquisition is fast and convenient, and the film development process is instead performed numerically on a personal computer.

Film-based holography was pioneered by Gabor [53]. Originally based on electronic waves, his work was later applied to optical frequencies by Leith and

Upatnieks. Holography (from the Greek words *holo*, "whole" and *graphe*, "writing") is a way of taking three-dimensional pictures on a film by recording an interference pattern that contains the complete (i.e., intensity and phase) spatial field scattered by an object. This film (or "hologram") can be later illuminated in such a way that the image of the object is perceived in three dimensions [54].

To record a hologram, a laser beam is often split into a first beam that scatters off an object of interest, and a second "reference" beam that interferes with the "unknown" scattered beam. The resulting interference pattern is recorded by a photographic film (Figure 3.1(a)). If one later views the film while it is illuminated by the same reference beam that was used in the recording process, a virtual thee-dimensional image of the original object is perceived by an observer (Figure 3.1(b)).

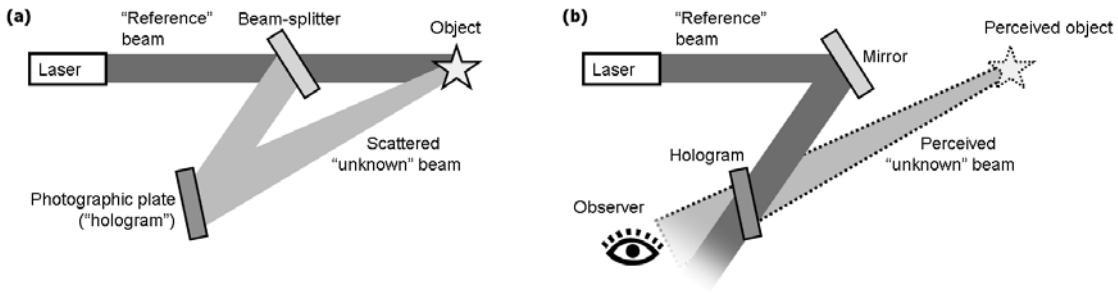

Figure 3.1. Setup for film-based holography. **(a)** Hologram recording. **(b)** Hologram observation.

3.1.2 Digital recording and reconstruction

In a digital holography setup, a digital camera replaces the film [55]. This not only offers a convenient and versatile setup, but also provides a detector that is much more linear with respect to the incident intensity than a photographic film. The recording

setup is practically unchanged compared to the film-based version, but the reconstruction process is quite different. The digital hologram captured by the digital camera is processed by a computer program to extract the intensity and phase distributions corresponding to the object. The exact algorithm that is used varies with the experimental setup: two common arrangements involve using collinear unknown and reference beams (on-axis configuration), or crossing them at a small angle (off-axis configuration).

3.1.3 Off-axis digital holography (Leith-Upatnieks configuration)

In off-axis digital holography, the unknown and reference pulses are crossed on the digital camera at an angle α [56], as depicted on Figure 3.2.

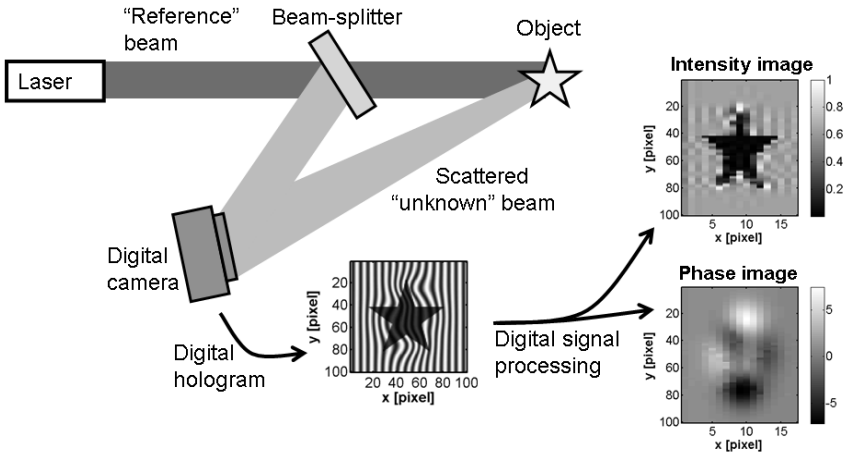

Figure 3.2. Setup for off-axis digital holography, showing the recording and reconstruction steps.

The digital hologram recorded under c.w. illumination (at frequency ω_0) and for a small crossing angle $\alpha \ll 1$ is:

$$H(x,y) = \left|E_s(x,y)\right|^2 + \left|E_r(x,y)\right|^2 + 2\left|E_s(x,y)E_r(x,y)\right|\cos\left(\varphi_r(x,y) - \varphi_s(x,y) + \frac{x\omega_0}{c}\alpha\right) \tag{3.1}$$

Equation (3.1) is the analog of Equation (2.2) in two dimensions with ω replaced by x, and τ by $(\omega_0/c)\alpha$. Thus, an algorithm similar to the one used in one-dimensional spectral interferometry can reconstruct the field of the unknown signal beam, $E_s(x,y)$ [32]. Briefly, this algorithm consists of the following steps:

- A two-dimensional Fourier transform is applied to $H(x,y)$ as shown on Figure 3.3.

- One of the interference terms is selected and inverse Fourier-transformed to yield $E_s(x,y)E_r(x,y)^*$.

- The reference field, $E_r(x,y)$, is divided from the remaining data to obtain $|E_s(x,y)|^2$ and $\varphi_s(x,y)$ as shown on Figures 3.4 and 3.5.

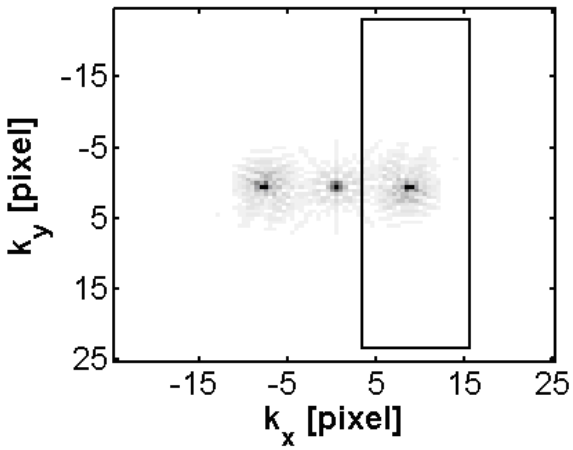

Figure 3.3. Two-dimensional Fourier transform of the digital hologram of Figure 2.2. The rectangle (black solid line) shows the region that is used to reconstruct the unknown image.

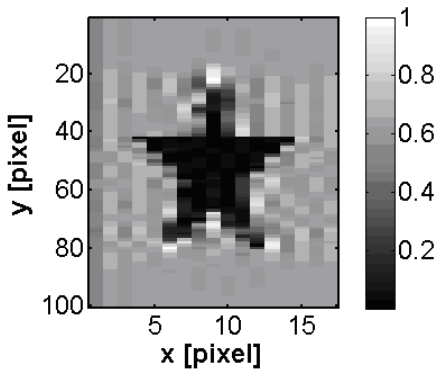

Figure 3.4. Intensity of the reconstructed unknown field.

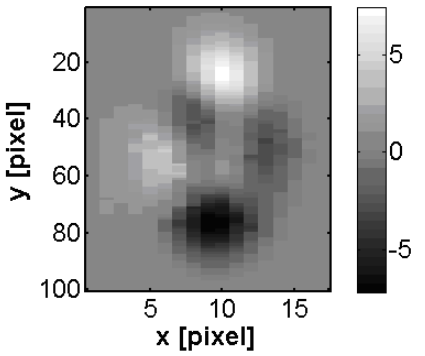

Figure 3.5. Unwrapped phase of the reconstructed unknown field.

The limitations encountered in Fourier-transform spectral interferometry (see Section 2.3.6) apply similarly to digital holography. In particular, one notices a reduced resolution due to Fourier filtering that only affects the x dimension (the unknown phase $\varphi_s(x,y)$ is reconstructed with the original spatial resolution along y). Note that Figure 3.5 displays the unwrapped phase, a delicate operation in two dimensions, in particular on experimental, noisy interferograms [57].

3.1.4 On-axis digital holography (Gabor configuration)

In the original configuration proposed by Gabor, the unknown and reference pulses interfere *collinearly*. Fourier filtering cannot be used to reconstruct $E_s(x,y)$ because of the absence of regularly-spaced fringes. One way to perform the reconstruction is to record multiple phase-shifted holograms [31, 58-60]. Another way is to use unknown and reference beams with different radii of curvature. In this case, a Fresnel transform can be used to reconstruct the unknown field [59, 61]. On-axis digital holography has found numerous applications in biomedical imaging of small structures because these objects naturally scatter diverging beams which are needed for the reconstruction algorithm [62].

3.2 Digital holography with ultrashort pulses

The basic concepts of digital holography presented above apply to c.w. light (with a very long coherence time), but they are easily extended to ultrashort pulses, or any other light sources with a short coherence time. One important consequence of the use of ultrashort pulses is the localization of the spatial fringes in time which reduces the fringe visibility.

Consider two ultrashort pulses $E_s(x,y,\omega)$ and $E_r(x,y,\omega)$ interfering at the camera at "zero delay" (i.e., $\tau = 0$). If the unknown pulse crosses the reference pulse at a small horizontal angle α, this introduces a small x-component in its wave vector, $k_{s,x} = [(\omega_0 + \omega)/c]\alpha$, and therefore the unknown pulse must be re-written as follows:

$$E_s(x,y,\omega) \rightarrow \exp\left[i(x\omega_0/c)\alpha\right]\exp\left[i(x\omega/c)\alpha\right]E_s(x,y,\omega) \tag{3.2}$$

Note that in Equation (3.2) and in most equations in this study, ω refers to the angular frequency measured with respect to ω_0. (See Ref. [22] for an explanation of this convention.) It is very instructive to compare Equation (3.2) with Equation (2.2) obtained for Fourier-transform spectral interferometry. In the case of pulses, crossing two beams at an angle α is not exactly equivalent to introducing an inter-pulse delay τ because of the additional phase term $(x\omega/c)\alpha$. This term results in a reduced fringe visibility as we will show in the next section and as shown in other texts [63].

3.2.1 Fringe visibility and coherence time

Because photo-detectors are slow square-law detectors, at each position they measure a time-integrated energy, or equivalently (because of Parseval's theorem) a frequency-integrated energy. Therefore the measured digital hologram is

$$H(x,y)=\int\left|E_s(x,y,\omega)\exp\left[i(x\omega_0/c)\alpha\right]\exp\left[i(x\omega/c)\alpha\right]+E_r(x,y,\omega)\right|^2 d\omega. \qquad (3.3)$$

For simplicity, we assume that there are no spatio-temporal couplings, so that the fields can be written as a product of a spatial function with a spectral function. We also assume that both pulses have the same spectral field which is uniform in the interval $[\omega_0 - \Delta\omega/2,\ \omega_0 + \Delta\omega/2]$. The measured hologram then reduces to

$$\begin{aligned} H(x,y)=&\left|E_s(x,y)\right|^2+\left|E_r(x,y)\right|^2 \\ &+2\,\mathrm{sinc}\left(\frac{\Delta\omega}{2}\frac{x}{c}\alpha\right)\left|E_s(x,y)E_r(x,y)\right|\cos\left(\varphi_r(x,y)-\varphi_s(x,y)+\frac{x\omega_0}{c}\alpha\right). \end{aligned} \qquad (3.4)$$

Equation (3.4) is the same as Equation (3.1) except for an additional factor corresponding to a decreased *visibility* of the fringes:

$$V(x) \equiv \mathrm{sinc}\left(\frac{\Delta\omega}{2}\frac{x}{c}\alpha\right) \tag{3.5}$$

The region where fringes are visible corresponds roughly to $|x| < 2\pi c/(\alpha\Delta\omega)$, resulting in a number of visible fringes equal to $\omega_0/\Delta\omega$, the number of optical cycles in a transform-limited pulse. For very short pulses, digital holographic measurements must therefore be spectrally resolved, or the spatial fringes will not be visible.

3.2.2 Fringe visibility and inter-pulse delay

When the unknown and reference pulses are longer than a few optical cycles ($\Delta\omega \ll \omega_0$), but separated in time by a delay $\tau \neq 0$, a similar situation arises: the visibility of the fringes decays with delay as $\mathrm{sinc}[(\Delta\omega/2)\tau]$. The physical interpretation is very clear: fringes will only be visible if the inter-pulse delay is less than the coherence time of the laser source. This property can be used to make "holographic movies" of fast events. For instance, researchers have used a series of a nanosecond pulses to generate multiple holograms in a single camera frame, resulting in a few snapshots of plasma dynamics. Each hologram was produced by a reference pulse that arrived at a different time and at a different angle [64]. The dependence of the fringe visibility with inter-pulse delay can also be used to compare the pulse-front of a distorted pulse with a reference pulse, for example to measure the pulse-front curvature introduced by lenses [65].

3.2.3 Fringe visibility and frequency

Although a zero (or very small) inter-pulse delay is necessary for spatial fringes to be visible, it is not sufficient. The unknown and reference pulses must also share common

frequencies ω; at each position, the visibility of the fringes is a function of the temporal and spectral *local overlap* of the two pulses. Although this dependence of the fringe visibility calls for some experimental care, it can also be used to detect couplings that may exist between space and time, or space and frequency.

Consider for instance an arbitrary unknown pulse, $E_s(x,\omega)$, and a reference field, E_r, that is not a pulse, but a *monochromatic* plane wave at $\omega = \omega_r$, i.e.:

$$E_r(x,\omega) = \delta_{\omega_r}(\omega). \tag{3.6}$$

In off-axis digital holography, these two fields are crossed at a small angle α and the interferometric term in Equation (3.3) that contains E_s becomes:

$$\int E_s(x,\omega)\delta_{\omega_r}(\omega) * \exp\left[i\frac{x\omega}{c}\alpha\right] d\omega \tag{3.7}$$

Because the reference beam is monochromatic, this integral simply reduces to:

$$E_s(x,\omega_r)\exp\left[i\frac{x\omega_r}{c}\alpha\right]. \tag{3.8}$$

As usual, Fourier filtering along the x coordinate can be used to reconstruct $E_s(x,\omega_r)$, which is the spectral component of $E_s(x,\omega)$ for the frequency ω_r. By simply scanning the frequency of the reference wave, it is therefore possible to observe couplings between the spatial characteristics of the pulse and its frequencies. It is even possible to completely reconstruct the spatio-temporal field $E_s(x,\omega_r)$ using a related method, called wavelength-scanning digital holography [52, 66] or sometimes Fourier-synthesis digital holography [67]. This method is presented in details in Section 3.4.

Because visible spatial fringes also require a common state of polarization between the unknown and reference beam, digital holography has also found applications in polarization imaging [68].

3.3 Self-referential measurements in digital holography

So far the nature of the reference pulse used in digital holography has not been explicitly discussed. Since the reference pulse needs to be coherent with the unknown pulse, a beam-splitter is often introduced in the laser beam *before* the "unknown" pulse is obtained, such as in Figures 3.1 and 3.2. In many cases, however, the reference pulse can be obtained from the unknown pulse itself using spatial filtering. If that is not possible, another technique called *spatial-shearing* interferometry can be used to measure the spatial field of the unknown pulse without an additional reference pulse.

The spatial filtering technique is the easiest to implement: a beam-splitter is inserted in the unknown beam *after* it is obtained, and one of the beams emerging from the beam-splitter passes through a spatial filter (usually a pinhole in the Fourier plane of a telescope; see Figure 3.6). The resulting reference beam is a plane wave (approximated experimentally by a large collimated beam), although any well-characterized beam can be used.

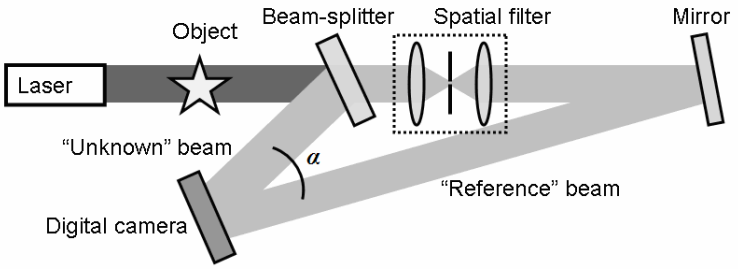

Figure 3.6. Self-referential digital holography setup with spatial filtering to generate the reference beam from the unknown beam.

An alternative to spatial filtering is simply to use a replica of the beam itself, but shifted (or "sheared") up or down by a small amount δy. If the unknown beam is $E_s(x,y)$, the "reference" beam is just $E_r(x,y) = E_s(x,y - \delta y)$. By crossing these two beams at a small horizontal angle and recording their digital hologram as in Figure 3.7, it is possible to numerically reconstruct their phase difference, $\varphi_s(x,y) - \varphi_r(x,y) = \varphi_s(x,y) - \varphi_s(x,y - \delta y)$. When δy is small compared to the scale of the changes in the spatial phase, this phase difference accurately approximates $\delta y\,(\partial\varphi_s/\partial y)(x,y)$. The unknown spatial phase $\varphi_s(x,y)$ is then obtained (up to an additional constant) by integration [25].

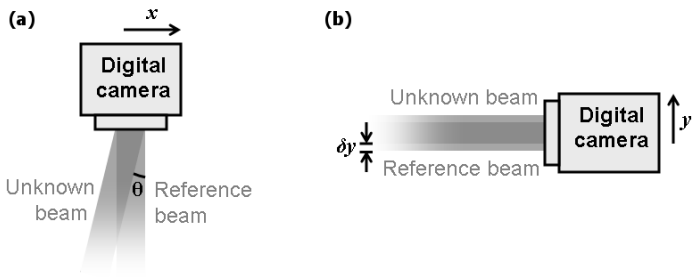

Figure 3.7. Setup for spatial-shearing digital holography. **(a)** Top view showing the two beams crossing at an angle θ. **(b)** Side view showing the vertical shear δy.

The resulting interferogram can be observed on a screen, or captured by a digital camera to obtain the digital holograms shown on Figure 3.8. Non-collimated beams, for example, result in a tilt of the spatial fringes; beam collimation can therefore be achieved by simple observation of the interferogram.

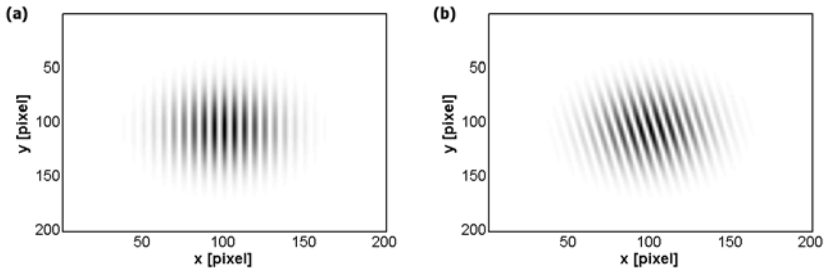

Figure 3.8. Simulations of spatial-shearing digital holograms. **(a)** Collimated beam. **(b)** Defocused beam.

3.4 Wavelength-scanning digital holography

As explained in Section 2.2, spectral interferometry and spatially-resolved spectral interferometry can be used to measure the two-dimensional spectral phase of an unknown signal pulse [69, 70]. With the introduction of a shear in space or in frequency [71-73], it is possible to perform a self-referenced measurement of the phase function $\varphi(x,\omega)$. Such measurements have also been reported using a combination of spectral interferometry and FROG [74], but no extension has been proposed to implement the full measurement of the pulse electric field in space and frequency, $E(x,y,\omega)$.

We show here that such a measurement can be performed using digital holography, extended to broadband laser sources. A related approach has been followed in the past: digital holographic measurements have been performed at different

wavelengths, sequentially [67], or simultaneously, both with continuous-wave and nanosecond-pulsed laser sources [75, 76], or at different times, on the picosecond time scale [77]. In these experiments, however, the phase function was not measured versus frequency (or time) and therefore they do not constitute a complete measurement of the electric field.

In this section we show how to combine a variation of Fourier-synthesis digital holography [78] with FROG to achieve true self-referenced three-dimensional measurements of the field of potentially arbitrary pulses, $E(x,y,t)$. We first discuss the theoretical foundations of the method, before applying it to experimental laser pulses with common spatio-temporal couplings, such as spatial chirp and pulse-front tilt.

3.4.1 Details of the method

Our method allows the measurement of the four-dimensional electric field, $E(x,y,z,t)$, of ultrashort pulses as they propagate through free space or known optical elements. First, because the electric field satisfies the wave equation, we note that it is sufficient to measure it at a given position $z = z_0$ along the propagation axis. Numerical integration, for example using the Fresnel transform, can later be used to numerically propagate forward (or backward) each monochromatic component by an arbitrary distance d. Therefore it suffices to measure the pulse for only one value of z, and hence we will suppress the z-coordinate in the rest of this study, and write the complex electric field as $E(x,y,\omega) \equiv \sqrt{S(x,y,\omega)}\exp[i\varphi(x,y,\omega)]$. Its inverse Fourier transform is $E(x,y,t) \equiv \sqrt{I(x,y,t)}\exp[i\phi(x,y,t)]$, which we approximate by a summation over discrete frequencies:

$$E(x,y,t)=\frac{1}{2\pi}\int_{-\infty}^{+\infty}\exp(+i\omega t)E(x,y,\omega)d\omega\simeq\frac{1}{2\pi}\sum_{k}\exp(+i\omega_k t)E(x,y;\omega_k)\delta\omega. \quad (3.9)$$

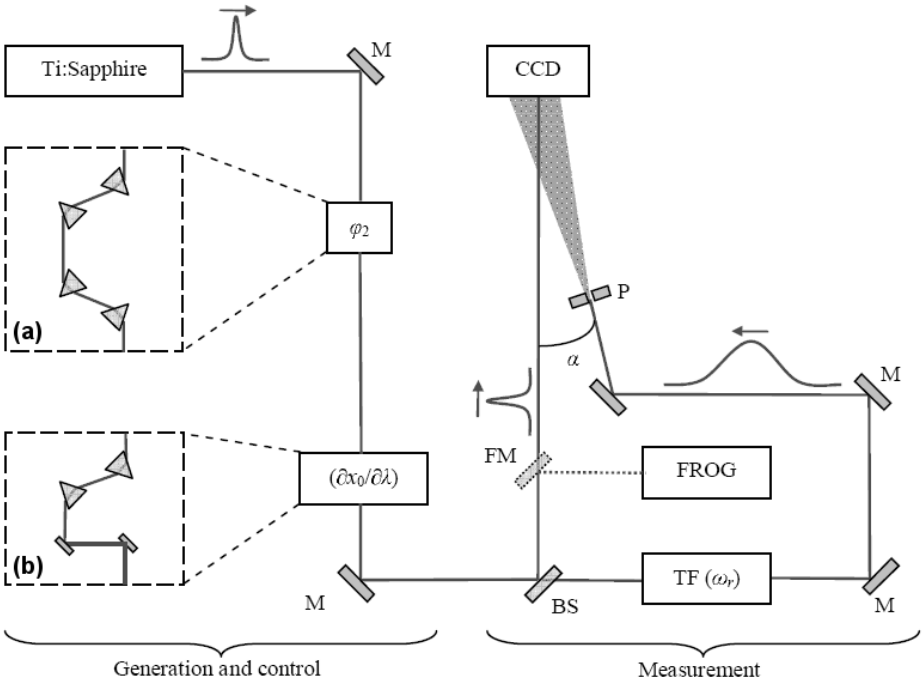

Figure 3.9. Schematic of the experiment: **(a)** four-prism second-order spectral phase (φ_2) control; **(b)** two-prism spatial chirp ($\partial x_0/\partial\lambda$) control; M, mirror; BS, beam-splitter; TF, tunable filter (band-pass) tuned to frequency ω_r; P, pinhole; FM, flip-mirror to perform the FROG measurement.

From a single digital holographic experiment one may at the same time isolate and measure an individual complex Fourier component $E(x,y;\omega_k)$. The principle of our experiment is depicted on Figure 3.9. A replica of the pulse to be measured is spectrally and spatially filtered by a narrow band-pass filter and a pinhole in order to obtain a quasi-monochromatic, quasi-planar wave in the far field. This wave interferes with the original pulse at an angle α, i.e., in the off-axis configuration of digital holography (see Section 3.1.3). Note that in this geometry, the original pulse is merely reflected a few times off

mirrors and beam-splitters, so that the device does not distort the input pulse. Following the naming convention of holography, we call the tilted, spherical wave the *reference wave* $E_r \equiv \exp(i\omega_r t)\sqrt{R}\exp\left(ix(\omega_r / c)\sin\alpha\right)$, and the original pulse the *signal wave* $E_s \equiv E(x,y,t) \propto \sum \exp(+i\omega_k t)\sqrt{S(x,y;\omega_k)}\exp(i\varphi(x,y;\omega_k))$. The resulting interferogram is recorded by a slow detector (a CCD camera) to form the digital hologram $H(x,y)$:

$$\begin{aligned} H(x,y) &\equiv \left\langle \left| E_r + E_o \right|^2 \right\rangle_t \\ &= R + \sum_k S(x,y;\omega_k) \\ &\quad + \left[\sqrt{R}\exp\left(ix(\omega_r / c)\sin\alpha\right)\sqrt{S(x,y;\omega_r)}\exp\left(-i\varphi(x,y;\omega_r)\right) + \text{c.c.} \right] \end{aligned} \tag{3.10}$$

Because of the time averaging $\langle\cdot\rangle_t$ performed by the CCD camera, all the cross-terms present in the expansion of $|E_r + E_s|^2$ vanish, except when $\omega_k = \omega_r$. Therefore, the last term in Equation (3.10), located at positive spatial frequency $u_r \equiv (\omega_r / c)\sin\alpha$ contains the intensity and (conjugated) phase $\sqrt{S(x,y;\omega_r)}\exp(-i\varphi(x,y;\omega_r))$ at frequency ω_r, and is easily isolated by the well-established reconstruction algorithm based on spatial Fourier transforms presented in Section 3.1.3.

By tuning the band-pass filter to other frequencies, we obtained the discrete set of intensity and phase functions, S and φ, necessary to fully characterize the electric field. But because these measurements are self-referenced, the absolute phase of $\varphi(x,y)$ is lost for each frequency ω_k, i.e., the spectral phase of the pulse is not measured. Therefore we perform an additional FROG measurement over a small spatial portion of the beam, to correctly set the relative phase of each Fourier component. A similar rephasing procedure has already been used in frequency-resolved wave-front measurements of ultrashort pulses [79]. It will be successful only if there exists a point (x_0,y_0) in the pulse where the

local spectrum $|E(x_0,y_0;\omega)|^2$ contains all the optical frequencies. As long as the beam spatial profile of each frequency extends over this point, this condition is satisfied, for example in the case of moderate amounts of spatial chirp presented below.

3.4.2 Experimental implementation

We measured the spatio-temporal profiles of trains of pulses generated by a mode-locked Ti:sapphire oscillator (KMLabs Inc.) with a typical bandwidth of 40 nm. The FROG measurements were performed with a single-shot second-harmonic FROG device (Swamp Optics 8-20) [80], which had a spectral resolution of 4 nm (see Table A.1). This determines the spacing $\delta\omega$ of the holographic measurements, as well as the upper bound of the bandwidth of the band-pass filter. We typically perform 20 measurements to cover the bandwidth of the oscillator (down to 5% of the spectrum peak), using four interference filters that we angle-tuned [81, 82]. The band-pass filters were stock items (CVI Laser) with central wavelengths (at normal incidence) of 780, 800, 807 and 835 nm. A 50-μm pinhole (Fort Wayne Wire Die, Inc.) spatially filters the resulting quasi-monochromatic wave.

Because two independent functions, $S(x,y)$ and $\varphi(x,y)$, are extracted from a single real-valued hologram $H(x,y)$, a loss of spatial resolution is unavoidable. When no additional frame is recorded to subtract the low spatial frequency term $R+\sum S(x,y;\omega_k)$, the optimal effective resolution is on the order of three times the size of a pixel. From a 13-μm-pitch camera (Pulnix TM-72EX) we obtained a resolution of 50 μm. From an experimental point of view, however, the low spatial frequency term is quite useful. By application of Parseval's theorem,

$$\sum_k S(x,y;\omega_k)\delta\omega \simeq \int_{-\infty}^{+\infty} I(x,y,t)dt \propto \left\langle I(x,y,t)\right\rangle_t. \tag{3.11}$$

Thus it appears that the second term in Equation (3.10), centered at zero spatial frequency, can also be isolated by the reconstruction algorithm, and may be used to measure the time-averaged intensity of the *entire* pulse. The location of each frequency component can thereafter be measured with respect to the center of the pulse intensity $\left\langle I(x,y,t)\right\rangle_t$, making the device much more tolerant to beam walk-off as the band-pass filter is angle-tuned.

Also, we would like to point out that it is unrealistic to approximate the reference wave in our configuration as a tilted plane wave. No matter how large the distance L from the pinhole to the camera, the reference wave will manifest a curved wave-front in addition to the tilt. A more precise approximation should therefore be $E_r = \exp(i\omega_r t)\sqrt{R}\exp[ix(\omega_r/c)\sin\alpha + i(x^2+y^2)\omega_r/(2Lc)]$. Thus the reconstruction algorithm will yield $\sqrt{S(x,y;\omega_r)}\exp[i\pi(x^2+y^2)\omega_r/(2Lc) - i\varphi(x,y;\omega_r)]$. The phase is contaminated by a pure quadratic term due to defocus, which is easily removed by calculating the projection of the measured phase $\varphi_m(x,y;\omega_r) = \pi(x^2+y^2)\omega_r/(2Lc) - \varphi(x,y;\omega_r)$ into the Zernike polynomial $2(x^2+y^2) - 1$ that corresponds to defocus and subtracting that term numerically [83, 84]. The advantage of using a pinhole, as opposed to a telescope with a large magnification for example, is that the former creates known intensity and phase reference profiles with minimal aberrations.

3.4.3 Experiments with couplings between space and frequency

To test our method, we generated pulses that exhibited a coupling between space and frequency, i.e., whose electric field cannot be written as $E(x,y,\omega) = f(x,y)g(\omega)$. This happens when cross terms $x\omega$ or $y\omega$ are present in the intensity $S(x,y,\omega)$, because of spatial chirp, or in the phase $\varphi(x,y,\omega)$, because of angular dispersion. We studied spatial chirp because an independent measurement was readily available in this case: a spatially-resolved spectrum is a measurement of $S(x,\omega)$ and therefore of spatial chirp along x.

Experimentally we introduced spatial chirp (without angular dispersion) in the beam with a pair of prisms in the arrangement shown in Figure 3.9. This results in a quasi linear variation of wavelength with position over the bandwidth of the oscillator.

We measured spatial chirp in two different ways: beam center position versus frequency (or wavelength), $x_0(\lambda)$ and $y_0(\lambda)$; and average frequency (or wavelength) at a fixed position, $\lambda_0(x,y)$. The change of the beam center position with wavelength is clearly illustrated in Figure 3.10, which also demonstrates the usefulness of the low-spatial-frequency term $\langle I(x,y,t)\rangle_t$ as a spatial reference. Our measurement matched very well the one obtained from a spatially-resolved spectrum.

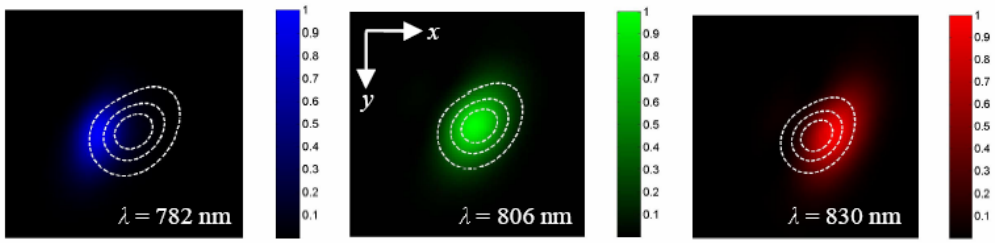

Figure 3.10. Plots of the intensity $S(x,y;\omega_k)$ of three spectral components, for ω_k corresponding to 782 nm, 806 nm and 830. The color scales represent the normalized intensities, and the dotted white lines are contour plots of the entire pulse intensity. This pulse exhibits a clear spatial chirp ($\partial x_0/\partial\lambda$).

3.4.4 Experiments with couplings between space and time

In the (x,y,t) domain, cross-terms xt or yt represent pulse-front tilt if present in the intensity term $I(x,y,t)$, and spatial chirp if present in the phase term $\phi(x,y,t)$. For pulses without focusing or angular dispersion, the (x,y,t) domain provides a very convenient way of displaying the complex electric field because the phase (derivative) yields the instantaneous wavelength $\lambda_{inst}(x,y,t) \equiv 2\pi c[\partial\phi(x,y,t)/\partial t]^{-1}$. Quite conveniently, variations of $\lambda_{inst}(x,y,t)$ with position reveal spatial chirp, and variations with time reveal temporal chirp, while a tilt in the shape of $I(x,y,t)$ is a signature of pulse-front tilt. Therefore, a colored surface plot (see Figure 3.11) can be used to display the complete two-dimensional (x,t) experimental profile of the complex electric field of well-collimated laser pulses (the $\partial/\partial t$ operator acting on the phase function removes time-independent spatial effects such as focusing).

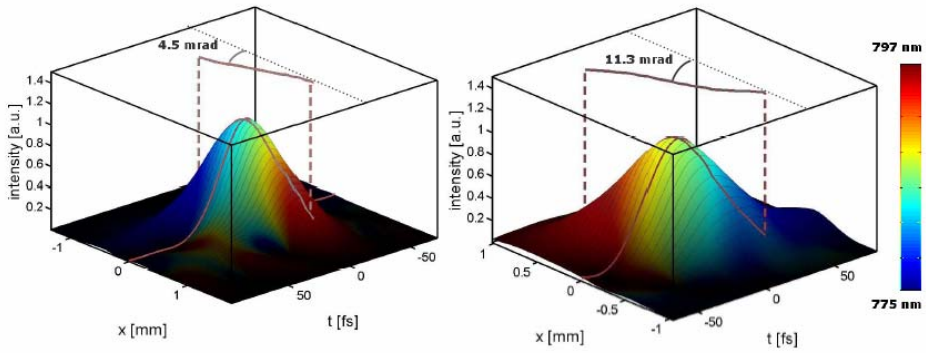

Figure 3.11. Profiles in the (x,t) domain of two ultrashort pulses. Both the vertical axis and brightness represent the intensity $I(x,t)$, while colors represent the temporal derivative of the phase, $\partial\phi(x,t)/\partial t$, converted to instantaneous wavelength. The solid gray lines that are projected onto the top of each cube correspond to the pulse-front $t_0(x)$. The angle of these lines with respect to a reference pulse-front (black dotted line) is a direct measurement of pulse-front tilt, measured in space (left: 4.5 mrad, right: 11.3 mrad).

To represent the complete experimental three-dimensional (x,y,t) intensity-and-wavelength profile of an ultrashort pulse, the most intuitive format is a movie so that space and time in the movie naturally represent the spatial and temporal evolution of an ultrashort pulse, respectively. A frame of such a movie is presented on Figure 3.12; the complete movie is available in one of our publications in an online journal [52] and can also be viewed at http://oe.osa.org/viewmedia.cfm?id=81166&seq=1.

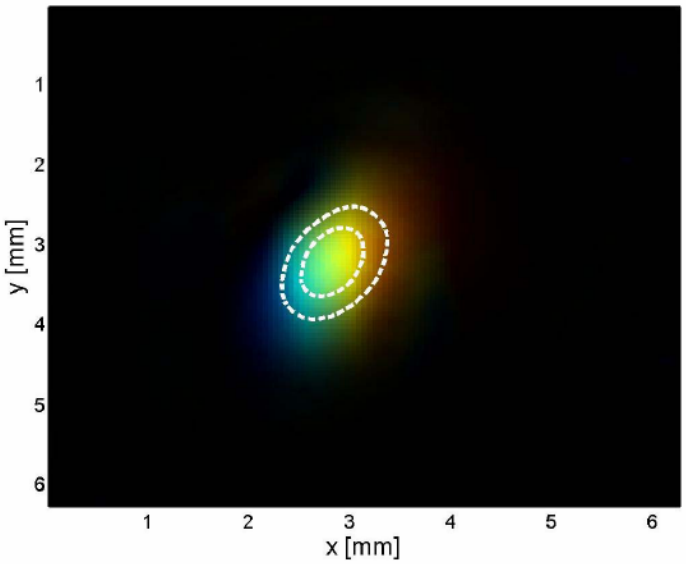

Figure 3.12. A frame from a movie representing the complete electric field $E(x,y,t)$ of a femtosecond laser pulse at a fixed time t. The color code is the same as in Figure 3.11. The complete movie is available at http://oe.osa.org/viewmedia.cfm?id=81166&seq=1.

3.4.5 Experiments at λ = 1.5 μm

We also implemented wavelength-scanning digital holography at $\lambda = 1.5$ μm, a wavelength largely used for telecommunication applications because of the existence of low-loss optical fibers in that spectral region [85]. Many elements of the 800-nm setup

have been replaced in order to have an optical setup compatible with standard telecommunication equipment, where optical fibers are ubiquitous.

Firstly, the laser source is an erbium-doped mode-locked fiber laser (MenloSystems TC-1550-B). The fiber is optically pumped by laser diodes at 980 nm and laser action occurs at 1567 nm, at the edge of the telecommunication C-band. The typical average power is 20 mW (13 dBm), or about one tenth of the typical average power of a Ti:sapphire oscillator. Passive mode-locking is achieved by a semi-conductor saturable absorber mirror (SESAM) [11, 86, 87] and results in ~300-fs pulses at a repetition rate of 26 MHz. Table 3.1 summarizes the differences between the Er:fiber laser and our standard Ti:sapphire laser.

Table 3.1. Comparison of the Ti:sapphire and Er:fiber mode-locked lasers used in this study.

Gain medium	Ti:sapphire	Er:fiber
Pump wavelength	532 nm (frequency-doubled Nd:YAG laser, or equivalent)	980 nm (laser diode)
Laser central wavelength	800 nm	1567 nm
Laser bandwidth (FWHM)	~40 nm	~8 nm
Transform-limit pulse duration	~30 fs	~300 fs
Mode-locking	Passive: Kerr lens	Passive: SESAM
Average power	~400 mW (typical)	~20 mW
Repetition rate	89 MHz	26 MHz
Polarization	Linear (horizontal)	Unpolarized

In addition to the laser source, the spectral filtering process that we use at 1.5 μm differs from the one used at 800 nm (which consisted of a set of interference band-pass filters that are angle tuned). We used an automated spectral shaper (Newport OSP-9100) that allows for an arbitrary modification of the spectral intensity. This device is based on a Texas Instrument chip containing an array of small micro-actuated mirrors [88]

illuminated by the input light dispersed by a diffraction grating. The spectral resolution is 0.1 nm, and the insertion loss of the device is below 7 dB. The spectral shaper is controlled over a serial interface and is programmed in LabView to generate a band-pass spectral filter with a tunable central wavelength and a bandwidth of 0.4 nm. Figure 3.13 shows the spectra recorded by a grating spectrometer when the central wavelength of the spectral shaper is tuned.

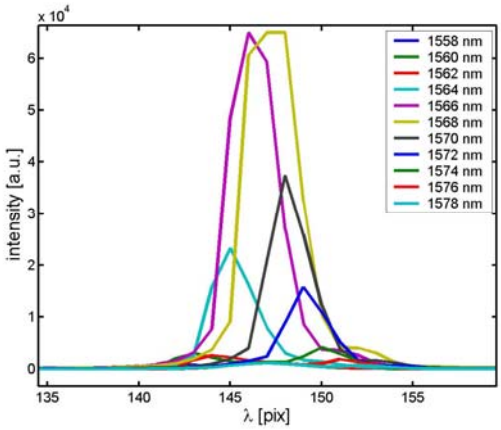

Figure 3.13. Spectra recorded by a grating spectrometer as the central wavelength of a band-pass filter (0.4 nm FWHM) is scanned by steps of 2 nm in a programmable spectral shaper. The horizontal axis was not calibrated since the central wavelength and bandwidth of the fiber laser are known.

At 1.5 μm it is not possible to use inexpensive CCD or CMOS silicon-based detectors; instead we used an InGaAs detector array (Oriel InstaSpec VI), limited to a one-dimensional geometry for cost reasons, but that allows detection in the 1.5-μm region.

Figure 3.14 shows a basic setup based on the elements described above that can be used to characterize the electric field of short pulses at 1.5 μm, as a function of *x* and

ω. The optical components are connected by standard single-mode fibers (Thorlabs SMF-28). If a two-dimensional InGaAs camera is available, such a setup could be use to fully characterize short pulses by reconstructing the full field, $E(x,y,\omega)$.

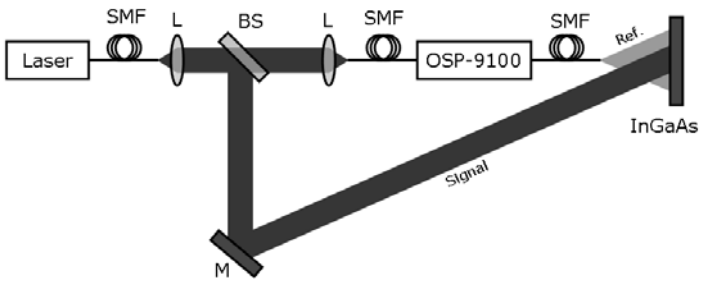

Figure 3.14. Basic setup to perform wavelength-scanning digital holography at 1.5 μm. **SMF**: single-mode fiber, **L**: lens, **BS**: beam-splitter, **M**: mirror, **OSP-9100**: programmable spectral filter (Newport) used as a tunable band-pass filter, **InGaAs:** photo-detector array (one-dimensional or two-dimensional). The pulse to be measured is generated in the signal arm, and interfered at the detector with the reference pulse.

The electric field $E(x,\omega)$ is obtained by recording the digital holograms as a function of x while the central wavelength of the band-pass filter of the programmable spectral shaper is scanned along the bandwidth of the pulse under test. This results in a "stack" of holograms (one for each wavelength during the scan), as shown on Figure 3.15.

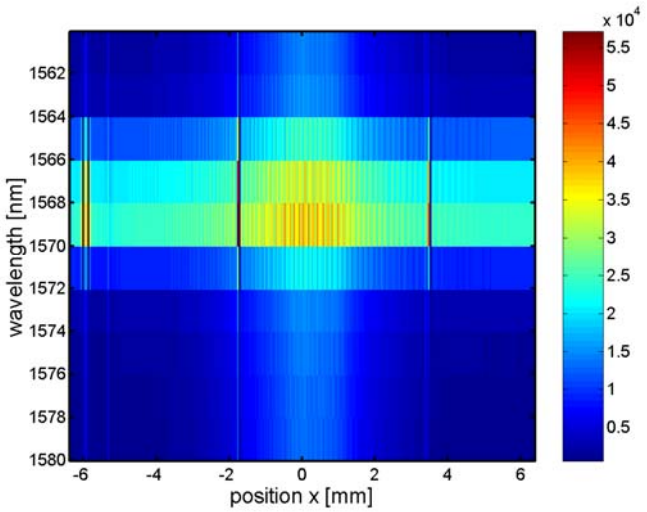

Figure 3.15. Stack of holograms as a function of position x (along which interference fringes are visible) and central wavelength of the programmed band-pass filter. The data is recorded by an InGaAs photo-detector array that contains a few malfunctioning elements resulting in dark vertical lines.

From the data on Figure 3.15, it is possible to fully reconstruct the electric field $E(x,t)$ of an unknown pulse, provided that its spectral phase is known at one position (e.g., at $x = 0$). Such a measurement can be performed with a FROG device (Swamp Optics 15-100; see Table A.1), which at 1.5 μm is based on the optical crystal proustite (Ag_3AsS_3, silver arsenic sulfide) [89].

3.5 Conclusions

Wavelength-scanning digital holography is a powerful and very general technique to measure the complete complex electric field of a train of ultrashort pulses. We have presented two implementations of this technique for femtosecond lasers at 800 nm and 1.5 μm. This method is well suited to the measurement of spatio-temporal distortions,

such as spatial chirp and pulse-front tilt. Such distortions are the lowest order distortions that may contaminate an ultrashort laser pulse, but the presented technique is naturally sensitive to higher-order spatio-temporal profiles.

However, because a wavelength scan is performed as the measurement is carried, this technique is limited to the characterization of trains of *identical* femtosecond pulses. Although such an assumption is usually satisfied in the case of mode-locked oscillators generating pulses of moderate energies, it is more questionable in the case of amplified femtosecond lasers, where shot-to-shot variations are not negligible and can even be problematic when nonlinear optical processes are involved. This issue is addressed in the next chapter where we present a related method allowing for a complete measurement of the electric field, $E(x,y,t)$, in a *single-shot* geometry.

CHAPTER 4

WAVELENGTH-MULTIPLEXED DIGITAL HOLOGRAPHY

The work presented in this chapter originally appeared in the following paper: [90] P. Gabolde and R. Trebino, *Single-shot measurement of the full spatio-temporal field of ultrashort pulses with multi-spectral digital holography*, Optics Express **14** (23) 11460-11467 (2006).

4.1 Measuring the complete spatio-temporal field

Wavelength-scanning digital holography, the method presented in Chapter 3, offers an original solution to the problem of completely measuring the spatio-temporal field of a femtosecond pulse. Such a method is especially useful to measure, for example, a pulse contaminated by spatio-temporal distortions introduced by optical elements (e.g., focusing elements). Our approach [52] extended the traditional two-dimensional information that is obtained from standard optoelectronic sensors using various techniques (linear and nonlinear spectral interferometry [69, 70, 73, 91], direct wave-front sensing [23, 24, 84], or two-dimensional digital holography [58, 61, 78]), by providing a three-dimensional measurement of the electric field. It is even possible to obtain a four-dimensional measurement (in free space) by using numerical methods to obtain the electric field dependence on the z-coordinate.

However, the scan of the wavelength that is required in our approach necessitates multiple frames of data to be recorded. This, in turn, requires a stable train of identical pulses. For low-intensity experiments, performed for example using mode-locked oscillators, this condition is usually satisfied. This requirement can be prohibitive,

however, for amplified laser systems that operate at very low repetition rates or have important shot-to-shot intensity fluctuations.

To overcome this limitation, we introduce in this chapter a device capable of measuring the complete three-dimensional spatio-temporal electric field $E(x,y,t)$ *on a single-shot*. Instead of recording multiple digital holograms for different wavelengths sequentially in time [52], we record them simultaneously in a larger two-dimensional camera frame. This large digital hologram contains all the necessary information to numerically reconstruct the full three-dimensional electric field $E(x,y,t)$. For that reason, we call our technique Spatially and Temporally Resolved Intensity and Phase Evaluation Device: Full Information from a Single Hologram (STRIPED FISH).

Setups for the simultaneous recording of a few holograms have been introduced in the past, but these involve a set of beam-splitters (or a special cavity) to generate a few replicas that must all be synchronized using delay lines [77]. As a result, they do not scale very well as the pulse becomes more complex in time (or frequency) and the number of necessary holograms increases. STRIPED FISH, on the other hand, involves a simple arrangement comprising only two main components that readily generate a large number of holograms. This configuration is more likely to scale to complex pulses in space and/or time. The multiple digital holograms are obtained by interfering the pulse under test with a well-characterized reference pulse or, alternatively, with a spatially-filtered replica of the pulse under test whose (spatially-uniform) spectral intensity and phase are measured by FROG. Thus STRIPED FISH is self-referencing, and should be ideal for low-repetition-rate systems.

4.2 Principle of wavelength-multiplexed digital holography

We first briefly recall how digital holography can be used to reconstruct the intensity and phase of the spatial electric field $E(x,y)$ of a monochromatic laser beam [61]. It involves crossing the "signal" beam (the beam to be characterized) and a "reference" beam (a pre-characterized beam) at a small angle α, for example in the vertical plane. One then measures the corresponding intensity $I(x,y)$, or "digital hologram", using a digital camera:

$$\begin{aligned} H(x,y) &= \left|E_s(x,y)\right|^2 + \left|E_r(x,y)\right|^2 \\ &\quad + E_s(x,y)^* E_r(x,y) e^{-iky\sin\alpha} + E_s(x,y) E_r(x,y)^* e^{+iky\sin\alpha} \end{aligned} \tag{4.1}$$

Because the last term of Equation (4.1) contains the modulation term $\exp[iky\sin\alpha]$, we may readily extract it from the measured intensity $I(x,y)$ using a well-established algorithm [32] that was introduced in Section 3.1.3. Assuming that we know the electric field of the reference pulse, $E_r(x,y)$, we can obtain the electric field of the signal pulse, $E_s(x,y)$, which contains both the spatial intensity ("beam profile") and the phase ("wave-front") of the beam.

A holographic technique generalized for broadband pulses/beams, rather than monochromatic beams, involves frequency-filtering the reference and signal pulses and generating monochromatic holograms for each frequency in the pulses (see Section 3.4.1). If we perform the reconstruction process at different frequencies ω_k spaced by $\delta\omega$, which satisfy the sampling theorem and which cover the bandwidth of the signal and reference pulses, we obtain the electric field $E(x,y)$ for each frequency ω_k. If the reference pulse's spectral phase is also known, it is then easy to reconstruct the signal field in the

frequency domain, which then yields the complete field in the time domain (Equation 3.9).

In contrast to multi-shot setups that rely on a scan of the wavelength to reconstruct $E(x,y,t)$ [52], STRIPED FISH only requires a single camera frame to do so. We still cross the signal and the reference pulses at a small vertical angle, but we additionally generate multiple digital holograms on a single camera frame to obtain the complete spatial and spectral dependence of the signal pulse in a simple single-shot geometry.

The principle of STRIPED FISH is illustrated on Figure 4.1. It involves generating multiple holograms, one for each frequency component in the pulse and then combining them to yield $E(x,y,\omega)$. Specifically, this entails interfering the signal pulse with the pre-characterized reference pulse at a small vertical angle α (about the x-axis) as in standard off-axis holography in the Leith-Upatnieks configuration (see Section 3.1.3). These two pulses then pass through a diffractive optical element (DOE) – equivalent to a low-resolution two-dimensional diffraction grating – which generates a two-dimensional array of replicas of the incident signal and reference pulses, yielding an array of holograms, all with horizontal fringes, where the beams cross. The second component of STRIPED FISH, a tilted interference band-pass filter or a Fabry-Pérot etalon, spectrally filters the beams into wavelengths that depend on the horizontal propagation angle [81, 82], because the band-pass filter is tilted by an angle β about the y-axis in the x-z (horizontal) plane. Finally, we also orient the two-dimensional diffraction grating so that it is rotated slightly by an angle φ about the optical axis z. As a result, the hologram array is also slightly rotated, so each hologram involves pairs of beams of a (uniformly spaced) different

wavelength. The resulting quasi-monochromatic holograms, each at a different color, yield the complete spatial field (intensity and phase) for each color in the pulse and can then be combined to yield the complete spatio-temporal field of the signal pulse, $E(x,y,t)$. A single camera frame is all that is required.

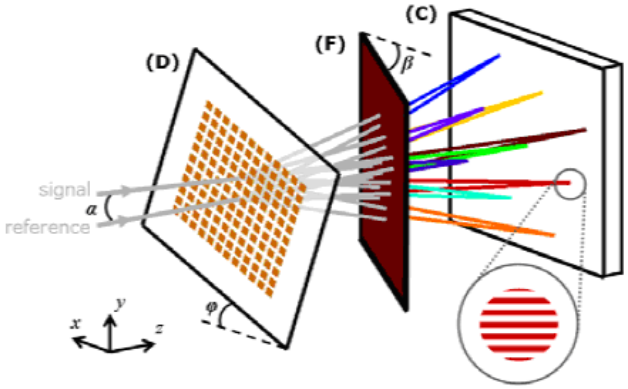

Figure 4.1. Three-dimensional view of STRIPED FISH. **(D)**: DOE; **(F)**: band-pass interference filter; **(C)**: digital camera. The signal and reference pulses are crossed at a small vertical angle α. The diffractive optical element (D) is rotated by an angle φ about the z-axis, and the filter (F) is rotated by an angle β about the y-axis. The inset shows one of the spatial interferograms ("digital holograms") captured by the digital camera.

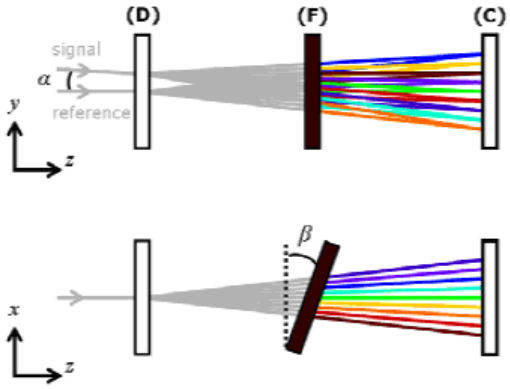

Figure 4.2. (Top) Side view (y-z plane) showing the signal and reference beams crossing at an angle α. **(Bottom)** Top view (x-z plane) showing how the frequencies transmitted by the band-pass filter increase with position x.

We choose the spatial period of the DOE to be much larger than the wavelength of the beams, so that many orders are diffracted at small and different angles. At the same time, we also choose the spatial period to be smaller than the beam spatial features that need to be resolved. As long as the bandwidth of the input beam is small compared to its central wavelength, angular dispersion within each diffracted order remains negligible.

4.3 Reconstruction of the electric field from a measured trace

To obtain the complex electric field $E(x,y,\omega)$, we apply a variation of the standard reconstruction algorithm to the measured STRIPED FISH trace (Figure 4.3). It involves first performing a two-dimensional Fourier transform of the STRIPED FISH trace. When the different holograms are well separated (Figure 4.3(a)), the only spatial fringes that are visible are the ones due to the small vertical crossing angle α between the signal and the reference pulses. Therefore, in the Fourier domain (Figure 4.3(b)), we expect to obtain one central region corresponding to the non-interferometric terms, and two other regions corresponding to the interferometric terms due to the crossing angle α. We only retain the upper region, which is the equivalent of the last term of Equation (4.1), and we inverse-Fourier-transform that region to obtain a complex-valued image (Figure 4.3(c)).

This image contains a collection of spectrally-resolved complex electric fields $E(x,y)$ measured at various frequencies ω_k, once we divide by the field of the reference pulse. These electric fields are distributed over the camera frame and need to be centered one by one. We use data from a reference experimental image obtained from a pulse free of spatio-temporal distortions to find the beam center corresponding to each spatial electric field, so that the data can be reorganized in a three-dimensional data cube,

$E(x,y,\omega)$. During this registration step, each digital hologram is assigned a frequency ω_k using calibrated data previously obtained by measuring the spectra of the various diffracted beams.

Finally, we apply Equation (3.9) to reconstruct the field $E(x,y,t)$ in the time domain. Using diffraction integrals, we can also numerically propagate the electric field through known elements along the z direction if desired, to attain the full four-dimensional spatio-temporal field.

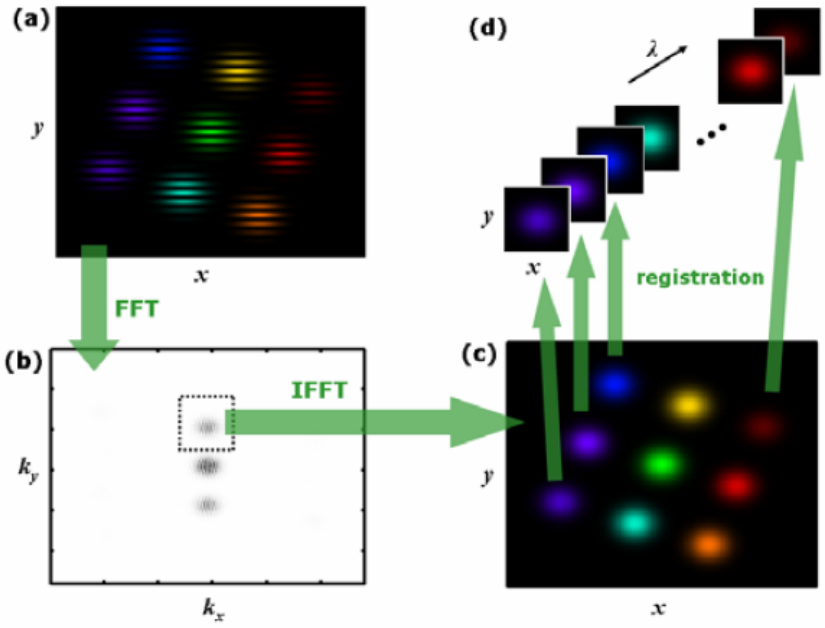

Figure 4.3. Algorithm used to reconstruct the three-dimensional electric field from a single camera frame. A two-dimensional fast Fourier transform is applied to a simulated STRIPED FISH trace **(a)**. The interferometric terms are selected in the Fourier plane **(b)**, and transformed back to the original x-y plane **(c)**. The resulting image contains both the spatial amplitude and phase, at the expense of a loss of vertical spatial resolution. A registration step is applied to center all the spatial distributions, and to assign the calibrated wavelengths, in order to obtain the multi-spectral complex data $E(x,y,\omega)$ **(d)**.

The spatial resolution of STRIPED FISH is limited by three effects: the angular dispersion introduced by the diffraction grating, the period of the grating itself, and the size of the filtering window in the Fourier domain. Although the two-dimensional grating introduces some angular dispersion within each digital hologram, slightly blurring the spatial profile of the beam, a very narrow band-pass filter may be used to reduce this effect (except in the case of extremely short pulses) at the expense of a decreased throughput. The period of the diffractive element also limits the spatial resolution, although the input beam can be expanded to compensate for that effect, as long as a large-area digital camera is used. Finally, the spatial resolution can also be limited by the size of the filtered window in the Fourier plane, limiting the spatial resolution to a few pixels. In practice we are restricted by this last effect.

Similarly, the spectral resolution is also controlled by two separate factors: the bandwidth $\delta\lambda$ of the band-pass filter, and the number N of holograms that fit on the digital camera. The latter is usually the limiting factor: the spectral resolution is then simply a fraction of the pulse bandwidth $\Delta\lambda/N$, where $\Delta\lambda$ is the input pulse bandwidth.

Note that it is possible to favor the spectral resolution by using more (but smaller) holograms, which will in turn decrease the spatial resolution. Conversely, one could favor the spatial resolution using larger (but fewer) holograms. Thus, there is a trade-off between spatial and spectral resolution. We can quantify the overall performance of STRIPED FISH with regard to beam/pulse complexity: in our case the maximum *time*-bandwidth product (TBP) that we can hope to measure is roughly equal to the number of holograms that are captured. Similarly, the maximum *space*-bandwidth product (SBP) is approximately equal to the number of spatial points obtained by the reconstruction

algorithm. In the end, the amount of information (number of independent data points), and therefore the maximum pulse complexity that our STRIPED FISH device can measure is estimated by introducing the *space-time-bandwidth product*, equal to TBP×SBP, which is on the order of 10^5 in our case. The space-time-bandwidth product may be increased by expanding the beam to be characterized, and by using a larger-area digital camera with a higher pixel count.

4.4 Experimental setup and results

4.4.1 Implementation as a Mach-Zehnder interferometer

As a proof of principle, we set up a STRIPED FISH device as a Mach-Zehnder interferometer (Figure 4.4). A first beam-splitter is used to separate an incident ultrashort pulse (800 nm) from a mode-locked Ti:sapphire oscillator (KMLabs Inc.) into a reference and a signal pulse. The pulse to be characterized is then obtained from the signal pulse before the two pulses are recombined on a second beam-splitter. This recombination is quasi-collinear: a small vertical angle α is introduced in order to generate horizontal fringes on the digital camera, where both pulses are temporally and spatially overlapped. The temporal overlap requires the use of an adjustable delay line (see Figure 4.4) that requires a careful adjustment to maximize the visibility of the interference fringes.

Between the second beam-splitter and the digital camera, we insert the rotated DOE and the tilted band-pass filter to generate the array of spectrally-resolved holograms. The coarse diffraction grating consists of an array of 10×10 μm reflective chrome squares, spaced by 50 μm, on the front surface of a quartz substrate. This optic can

be used in transmission or in reflection if dispersion from the substrate must be avoided. The interference band-pass filter (CVI Lasers) has a nominal wavelength $\lambda_n = 837$ nm and a bandwidth (FWHM) of 3 nm, and we tilt it by an angle $\beta \sim 20°$ to transmit the pulses centered at 800 nm. We typically generate an array of a least 20 holograms, which are captured by a high-resolution (5-megapixel) CMOS camera (2208×3000 PixeLINK PL-A781). The wavelength corresponding to each interferogram is calibrated by measuring the local spectrum at that point using a fiber-coupled grating spectrometer (Ocean Optics USB2000).

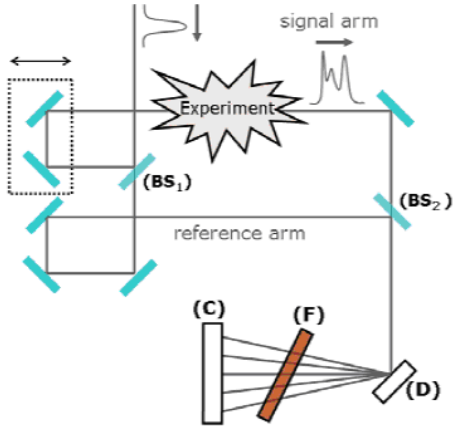

Figure 4.4. Mach-Zehnder interferometer used to implement our STRIPED FISH device, drawn in the *x*-*z* plane. **(BS$_{1,2}$)**: beam-splitters. **(D)**: DOE. **(F)**: interference band-pass filter. **(C)**: digital camera. The optical paths of both arms are matched using the delay stage, and a small vertical angle is introduced between the signal and reference pulses so that horizontal fringes are obtained on the digital camera.

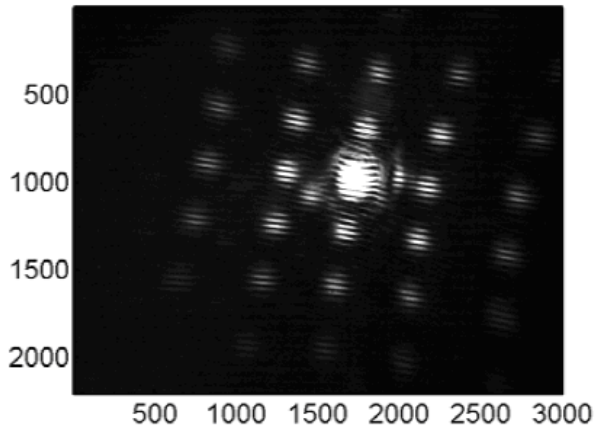

Figure 4.5. Typical experimental STRIPED FISH trace (2208×3000 pixels) obtained with a 5-megapixel CMOS camera. The central digital hologram is saturated because of the absence of anti-reflection coating on the DOE substrate used away from Brewster's angle.

Figure 4.5 shows a typical STRIPED FISH trace. The central interferogram, corresponding to the undiffracted order of the DOE, is much more intense than the other holograms. This is due to the lack of anti-reflection coatings on the stock substrate (quartz) of the DOE. When possible, we try to minimize this effect by using signal and reference pulses with horizontal polarizations and incident on the DOE at Brewster's angle. For a DOE fabricated on a quartz substrate, Brewster's angle $\theta_B = \mathrm{Arctan}(n_{\mathrm{DOE}})$ corresponds to $\theta_B \simeq 57°$. An example of a STRIPED FISH trace recorded at Brewster's angle is shown on Figure 4.6. Compared to Figure 4.5, the brightness of the central (undiffracted) hologram is greatly reduced, and all the digital holograms can be simultaneously recorded within the dynamic range of a 10-bit digital camera. Note that there is a weak reflection present on the right of the central hologram; it is due to a reflection from the *back* surface of the DOE substrate and could be easily removed by an index-matching element.

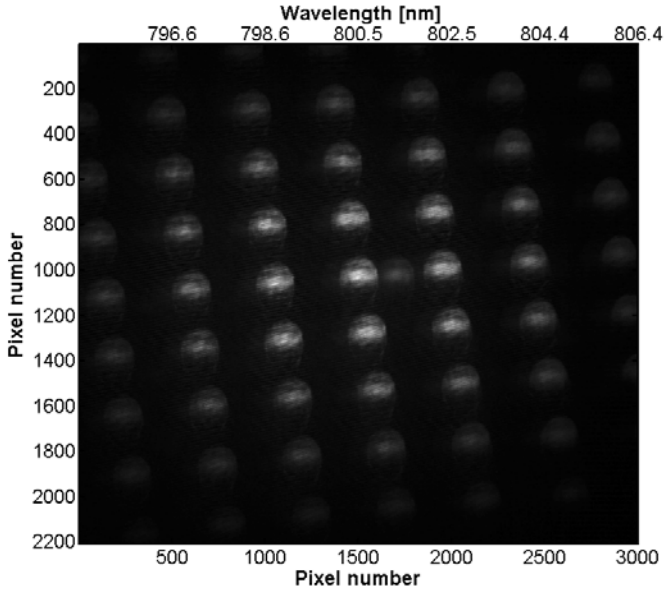

Figure 4.6. Experimental STRIPED FISH trace recorded at Brewster's angle.

We demonstrate our technique using ultrashort pulses from a mode-locked Ti:sapphire oscillator. The pulses are centered at 800 nm and have approximately 30 nm of bandwidth (FWHM). Because of the high repetition rate (89 MHz) of the laser, our measurement averages over many pulses, but our STRIPED FISH device uses a single-shot geometry, and no scanning occurs. With our 1-kHz chirped-pulse amplified system, recording single-shot STRIPED FISH traces was straightforward, however, since sub-millisecond exposure times are readily obtained by digital cameras.

4.4.2 Measurement of the spectral phase

We now show that our STRIPED FISH device is sensitive to the spectral phase of the signal pulse. We introduce some group delay in the signal pulse by delaying it with

respect to the reference pulse. This modifies the absolute phase of the fringes of each digital hologram in the experimental STRIPED FISH trace.

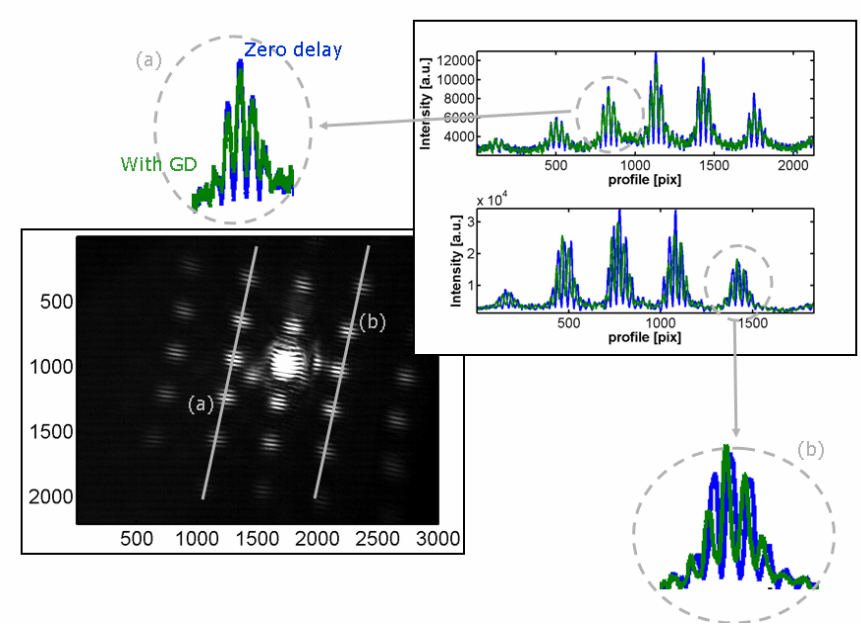

Figure 4.7. Encoding of the spectral phase in a STRIPED FISH trace. The lower left image is a STRIPED FISH trace. Two profiles are recorded along the gray lines, and graphed on the upper right plot. The insets show the profile of two holograms **(a)** and **(b)** recorded at two different wavelengths. Blue curves: zero delay. Green curves: group delay introduced in the signal pulse.

Figure 4.7 depicts the situation. The lower left image corresponds to a STRIPED FISH trace, from which two profiles (gray lines) are extracted. These two profiles are shown using two blue curves on the upper right graph. These profiles are recorded at zero delay between the reference pulse and the signal pulse. A small group delay is then introduced in the signal pulse by slightly translating the delay line of the Mach-Zehnder interferometer. The corresponding STRIPED FISH trace looks very similar to the one of

Figure 4.7, except for the absolute position of the spatial fringes: if the same profiles are extracted from the trace along the gray lines, the curves in green are obtained. A careful inspection of two interferograms – labeled (a) and (b) – reveals that there is a relative phase shift that is introduced by the group delay.

This fringe shift is recorded as a function of frequency, and corresponds to the spectral phase of the signal pulse (measured with respect to the reference pulse). As expected, a linear spectral phase characteristic of group delay is obtained (Figure 4.8(a)).

A similar experiment can be performed by introducing a dispersive window in the signal arm of the interferometer, so that group-delay dispersion (GDD) is introduced in the spectral phase of the signal pulse. The same procedure is repeated, and a characteristic quadratic spectral phase is obtained experimentally (Figure 4.8(b)).

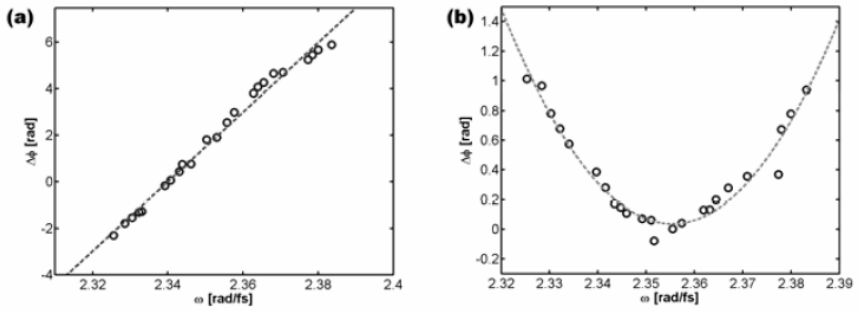

Figure 4.8. (a) Fringe shift in each digital hologram as a function of frequency, showing a linear phase due to group delay. Open circles: measurement; dotted line: linear fit. **(b)** Fringe shift in each digital hologram as a function of frequency, showing a quadratic phase due to group-delay dispersion. Open circles: measurement; dotted line: quadratic fit.

4.4.3 Measurement of spatio-temporal couplings

We now show the reconstructed field of a pulse with horizontal spatial chirp. We introduce spatial chirp in the signal beam using a pair of gratings. Figure 4.9 shows two slices of the reconstructed electric field $E(x,y,t)$ that are obtained in this measurement; one slice is obtained at $y = 0$ (Figure 4.9(a)), and the other at $x = 0$ (Figure 4.9(b)). In these plots, the instantaneous wavelength is calculated from the derivative of the temporal phase. Any temporal gradient of the instantaneous wavelength corresponds to temporal chirp, and any spatial gradient is due to spatial chirp. Horizontal spatial chirp is clearly visible on Figure 4.9(a).

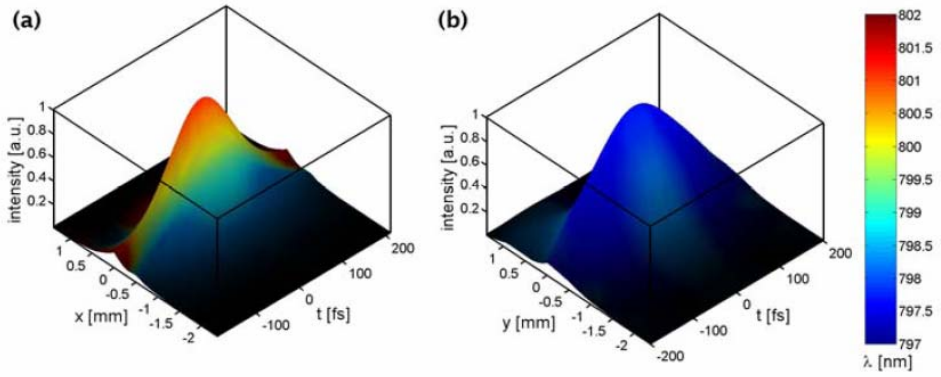

Figure 4.9. (a) *x-t* slice of the measured electric field $E(x,y,t)$ of a pulse with spatial chirp. The vertical axis shows the electric field intensity $|E(x,t)|^2$ and the color shows the instantaneous wavelength derived from the phase $\varphi(x,t)$. The spatial gradient of color shows the spatial chirp along the *x* direction. **(b)** *y-t* slice of the same measured electric field. No spatial chirp is present along the *y* direction, as expected.

In the aforementioned proof-of-principle experiments, the Ti:sapphire oscillator pulse was used as the reference pulse, and a replica of that pulse was distorted in order to

create an interesting pulse for demonstration purposes (see Figure 4.4). The reference pulse was therefore spatially smooth, and had an approximately flat spectral phase. However, in most cases it is possible to perform a fully *self-referenced* measurement of the distorted signal pulse by spatially-filtering *that* pulse. The resulting pulse then has a well-defined (i.e., smooth) spatial profile, and its spectral intensity and phase may be readily characterized using a single-shot FROG device [80], so that it may be used as the reference pulse in the STRIPED FISH technique. This self-referencing implementation of STRIPED FISH is presented in Section 4.6.

4.5 Design of the DOE

The essential component of our STRIPED FISH device is the two-dimensional diffraction grating that we use to generate multiple replicas of an input beam. In this section, we describe the choice of the design parameters and the fabrication process of this element.

For clarity, we first describe the action of the diffractive optical element (DOE) in one dimension (x). The DOE is an array of reflective squares on a quartz substrate. The corresponding one-dimensional transfer function $D(x)$ is represented on Figure 4.10; a is the width of each square and b is the square separation distance.

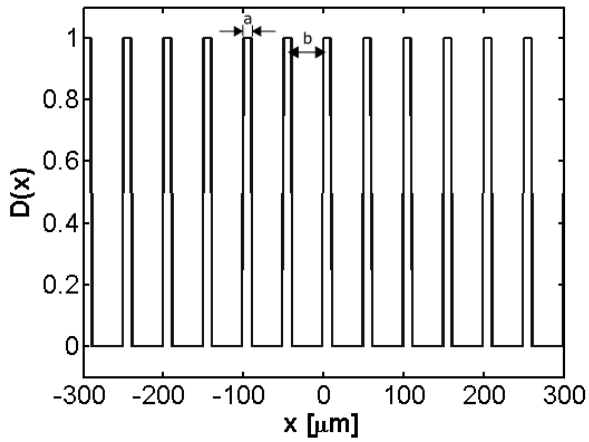

Figure 4.10. One-dimensional representation of the transfer function $D(x)$ of the DOE; a is the size of each square, and b is their separation. Typically, a = 10 μm and b = 50 μm.

4.5.1 Working distance

Clearly, a DOE with the reflectivity function $D(x)$ pictured on Figure 4.10 acts as a reflective grating of spatial period b. Thus, under an angle of incidence θ_B equal to Brewster's angle, multiple orders are diffracted in directions θ_m given by the grating equation:

$$\theta_m(\lambda) = \mathrm{Arcsin}\left(\frac{m\lambda}{b} + \sin\theta_B\right) - \theta_B \tag{4.2}$$

In Equation (4.2), m is the order of diffraction, and the angle of the diffracted order m is measured with respect to the specular reflection ($m = 0$). These angles are defined in the far field of the DOE, i.e., at a distance z larger than its Fraunhofer distance [92]:

$$z \gg \frac{b^2}{\lambda_0} \tag{4.3}$$

Additionally, we also require that the diffracted beams do not overlap after a distance z, where the digital camera is placed. For an input beam of size w, this geometrical condition requires that:

$$z > \frac{bw}{\lambda_0} \tag{4.4}$$

Obviously, for the DOE to perform well, a large number of spatial periods b must be illuminated by the input beam of size w (i.e., $w \gg b$). Therefore satisfying Equation (4.4) ensures that Equation (4.3) is satisfied.

To the lower bound of z set by Equation (4.4), we must also add an upper bound set by the Rayleigh range of the input beam. To avoid self-diffraction effects from this beam, we require that:

$$z \ll \frac{w^2}{\lambda_0} \tag{4.5}$$

To conclude, the working distance of the DOE is given by the following range for z:

$$\frac{bw}{\lambda_0} \ll z \ll \frac{w^2}{\lambda_0} \tag{4.6}$$

Note that the working distance given by Equation (4.6) also holds for the case of a two-dimensional DOE.

Figure 4.11 shows the effect of the DOE on a Gaussian beam (beam size $w \simeq 3$ mm) after a free-space propagation of 10 cm and 50 cm, for three different

wavelengths (750 nm, 800 nm, 850 nm) and for a spatial period $b = 50$ μm with $b/a = 5$. The initial near field interference effects quickly result in well-separated diffracted orders. Indeed, for this case the working distance is given approximately by 20 cm $\ll z \ll$ 1000 cm.

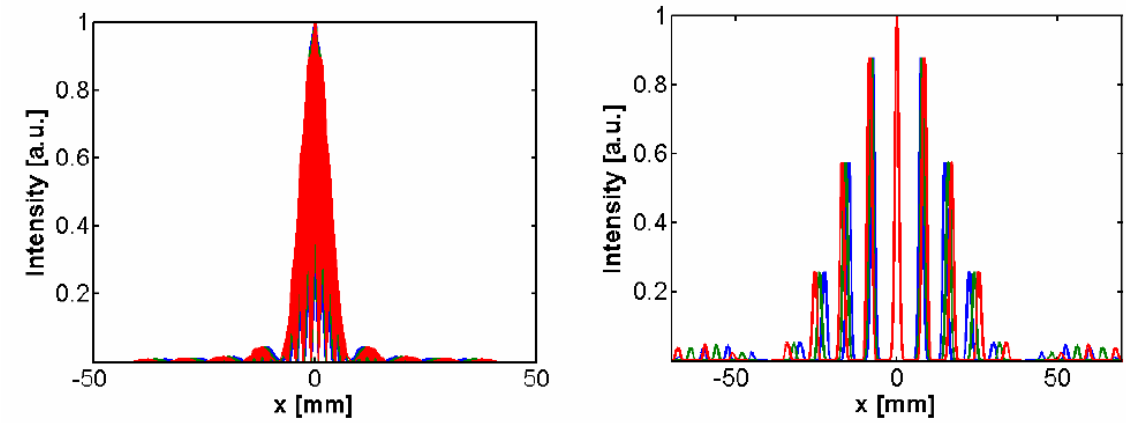

Figure 4.11. Free-space propagation of a 3-mm Gaussian beam reflecting off the DOE, after 10 cm **(left)** and 50 cm **(right)**, for three different wavelengths (blue: 750 nm; green: 800 nm; red: 850 nm).

4.5.2 Diffracted orders efficiency

As with any diffraction grating, the relative efficiency with which the orders are diffracted in the far field depends on the shape of one individual spatial period. In the case of the reflection function $D(x)$ of Figure 4.10, the efficiency function is given by the magnitude of the Fourier transform of a rectangle of length a, i.e., a sinc^2 function with a characteristic width of $1/a$. The characteristic shape of a sinc^2 curve is clearly visible in the envelope of Figure 4.11.

This efficiency curve determines the number of "useful" diffracted orders, i.e., orders that are efficiently diffracted. In one dimension, this number is roughly given by

the ratio b/a. In two dimensions, this number becomes $(b/a)^2$. Larger ratios result in an increase in the number of useful diffracted orders, but reduce the overall efficiency of the DOE. Thus, there is a trade-off between the number of holograms on a STRIPED FISH trace, and the device efficiency, or equivalently, between the spectral resolution and the throughput, a situation comparable to the case of an imaging spectrometer equipped with an adjustable slit.

4.5.3 Choice of a matching interference band-pass filter

On Figure 4.11, it is clear that the diffracted orders suffer from angular dispersion and spatial chirp: within a diffracted order $m \neq 0$, the frequency components of the original input beam are centered at different positions along the x axis. This dispersive property – the basis of grating spectrometers – may seem at first sight problematic in our application. This effect, however, is mitigated by the use of the spectral filter immediately after the DOE, and in practice does not affect our measurements, except in the case of extremely broadband pulses where successive orders start to overlap (in which case a DOE cannot be used).

According to the principle of operation of STRIPED FISH described in Section 4.2, the spectral filter must pass a different wavelength for each diffracted order m. After free-space propagation from the DOE, each order has a different center position, and a different angle θ_m. To spectrally resolve the diffracted orders, one must therefore use a band-pass filter whose transmitted wavelength depends on position, or angle. For narrow bandwidth pulses ($\Delta\lambda/\lambda_0 \ll 1$), we use the angle-tuning property of interference band-pass filters. If an interference band-pass filter has a nominal central wavelength λ_n and is

tilted by an angle β, then the wavelengths transmitted by the band-pass filter for each order m are given by [81, 82]:

$$\lambda_t^{(m)} = \lambda_n \left(1 - \frac{(\beta - \theta_m)^2}{2\mu^2} \right), \tag{4.7}$$

where μ is the effective refractive index of the interference filter [93]. This relation is valid for angles up to ~20°: for larger angles, the transmitted wavelength starts to depend on the light polarization. In this study, we limit ourselves to the *p* polarization (parallel to the plane of incidence, and usually in the plane of the optics table), and to angles up to ~30° to avoid an excessive increase in the filter bandwidth [81]. As an example, Figure 4.12 shows the wavelengths that are transmitted by an interference band-pass filter with a nominal wavelength λ_n = 820 nm and a transmission bandwidth of 3 nm (FWHM). In this experiment, the diffracted orders are generated by a two-dimensional diffraction grating with a spatial period b = 10 μm. The diffraction profile is shown on the inset of Figure 4.12. The spectra of four diffracted orders (labeled A,B,C,D) are recorded with a fiber-coupled grating spectrometer (Ocean Optics USB2000).

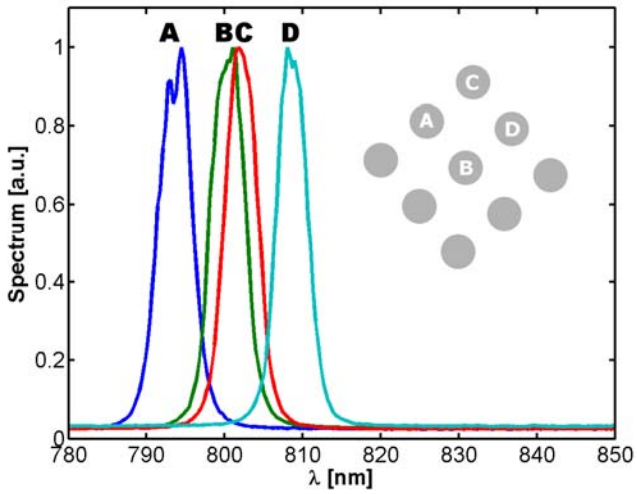

Figure 4.12. Spectra from a two-dimensional diffraction grating (b = 10 μm) and a tilted interference band-pass filter. The inset shows the locations of the diffracted beams in the far field.

This experiment shows that a tilted band-pass interference filter is well suited to spectrally resolve pulses with a bandwidth of a few to several tens of nanometers. It is not clear, however, how large a bandwidth it can support, so we now describe how to estimate an upper bound on that parameter.

For a typical value of $\mu = 1.45$, an angle $\beta - \theta_m$ of 30° gives in Equation (4.7) a maximum normalized blue shift of:

$$\left.\frac{\lambda_n - \lambda_t}{\lambda_n}\right|_{\max} \simeq 6\% \tag{4.8}$$

The longest wavelength that can be passed in this configuration is therefore λ_n (for $\theta_m = \beta$); β in chosen in accordance with Equation (4.7) so that the central wavelength is λ_0 (for $\theta_0 = 0$), the central wavelength of the pulse. The spectral content that can be resolved in this manner is therefore limited to ~$2\times(\lambda_n - \lambda_0)$. According to Equation (4.5), this limits

the maximum pulse bandwidth to less than ~6% of its central wavelength (i.e., less than 50 nm at 800 nm). For larger pulse bandwidths it is possible to use a linear variable interference band-pass filter where the passed wavelength depends on the transverse position x (e.g., Schott VERIL VIS-60).

To match the design of the DOE to the characteristics of an interference band-pass filter (or vice-versa), we must satisfy two conditions: (i) the wavelengths transmitted by the filter must cover the spectral content of the input pulse (i.e., two or three times its bandwidth $\Delta\lambda$), and (ii) the number of diffracted orders must be equal to the covered spectral range divided by the desired spectral resolution, $\delta\lambda$.

Let us consider the first condition. According to Equation (4.7), the longest wavelength that is passed by the filter is given by:

$$\lambda_{\max} = \lambda_n \left(1 - \frac{\left(\beta - \theta_{\max}\right)^2}{2\mu^2} \right) \tag{4.9}$$

In Equation (4.7), β is chosen so that the undiffracted order $m = 0$ is passed with the central wavelength of the pulse λ_0, i.e.:

$$\lambda_0 = \lambda_n \left(1 - \frac{\beta^2}{2\mu^2} \right) \tag{4.10}$$

Since the number of diffracted orders (in one dimension) is given approximately by b/a, we approximate $m_{\max}$ by $b/(2a)$ to estimate a value for $\theta_{\max}$:

$$\theta_{\max} \simeq \operatorname{Arcsin}\left(\frac{\lambda_0}{2a} + \sin\theta_B \right) - \theta_B \tag{4.11}$$

To simplify this equation, we assume that $\lambda_0 \ll a$. We will show later that this assumption is consistent with the narrow bandwidth approximation ($\Delta\lambda \ll \lambda_0$). In this case we obtain simply $\theta_{max} \simeq \lambda_0/(2a)$. Note that while the diffracted angles of the various orders depend on b in Equation (4.2), the largest diffracted angle depends on a (because there are about b/a diffracted orders).

The spectral content covered by the filter is then:

$$\lambda_{max} - \lambda_{min} \simeq \lambda_0 \frac{2\beta\theta_{max}}{\mu^2} \simeq \frac{\lambda_0^2}{a}\frac{\beta}{\mu^2} \tag{4.12}$$

A simple calculation shows that the bandwidth that can be covered by the filter is given by:

$$\frac{\Delta\lambda}{\lambda_0} \simeq \frac{\lambda_0^2}{a^2\mu^2} \tag{4.13}$$

This result indicates that the DOE parameter $1/a^2$ controls the (normalized) bandwidth that the system can support in one dimension. Equation (4.13) also applies unchanged to the two-dimensional case because adding the other transverse dimension to the problem does not affect the value of θ_{max}.

Now let us consider the second condition regarding the desired spectral resolution $\delta\lambda$ of the system. We assume that the bandwidth of the interference filter is smaller than $\delta\lambda$, even under an oblique incidence. In that case, $\delta\lambda$ is simply given by the spectral range (~$2\Delta\lambda$) divided by the number of diffracted beams. In the two-dimensional case, we obtain:

$$\frac{\delta\lambda}{\Delta\lambda} \simeq \frac{2a^2}{b^2} \tag{4.14}$$

To compare with Equation (4.13), we can also normalize the spectral resolution by the central wavelength to obtain:

$$\frac{\delta\lambda}{\lambda_0} \simeq \frac{2\lambda_0{}^2}{b^2\mu^2} \tag{4.15}$$

To summarize, Equation (4.13) and (4.15) can be used to choose the parameters *a* and *b* of the DOE to obtain a desired spectral range and spectral resolution. To satisfy the working distance requirement of Equation (4.6), it might therefore be necessary to change the input beam size *w* using a telescope or a 4-*f* imaging system. Alternatively, it is possible to image the beams diffracted by the DOE so that the diffracted angles match the values required by a given interference band-pass filter.

4.5.4 Fabrication of a custom DOE

Because an optimal DOE requires a careful choice of the design parameters *a* and *b*, it is unlikely that stock two-dimensional diffractions gratings (e.g., Max Levy FA079, Thorlabs BPD254-FS) satisfy the conditions set forth by Equations (4.6), (4.13) and (4.15). To allow for more flexibility, we chose to design our own custom DOE.

Fortunately, this optical element closely resembles photo-masks (also called reticles) that are used in the micro-electronics industry [94]. As a fortunate consequence, customs photo-masks are inexpensive to fabricate. They typically consist of a transparent substrate (soda lime or quartz) on which a layer (iron oxide or chromium) opaque to UV light is patterned by electron-beam lithography. For our application, we choose

chromium, a metal opaque in the UV (the spectral region normally used with photo-masks) but partially reflective in the near IR.

We design our photo-masks using industry-standard CAD tools such as Cadence Virtuoso or AutoCAD. The design files are converted to a format that is understood by a pattern generator that writes the pattern on the DOE substrate. Feature sizes on the order of a few microns were easily obtained during the fabrication of such masks both on site (Georgia Tech Micro-electronics Research Center) and in an external company (Photo Sciences Inc.).

4.6 Fully self-referenced STRIPED FISH

The setup presented in Figure 4.4 is not completely self-referenced because the pulse to be measured (the "signal" pulse) is generated *within* the Mach-Zehnder interferometer upon which STRIPED FISH is built. Furthermore, the spectral phase of the signal pulse was not measured: only changes of that spectral phase from one experiment to the next were measured, for example in Figures 4.7 and 4.8.

In this section, we present another implementation of STRIPED FISH that is fully self-referenced. This device requires only one input pulse, the pulse under test. This pulse is split into two replicas, one of which is spatially filtered to result in a reference pulse (a pulse whose *spatial* phase is essentially constant). The *spectral* phase of that reference pulse is therefore free of any spatial dependence, and is measured by a FROG device (e.g., GRENOUILLE) matched to the pulse characteristics [80, 95]. This completely characterizes the reference pulse that can then interfere with the signal pulse in the usual

configuration (two-dimensional diffraction grating followed by a spectral filter and a digital camera).

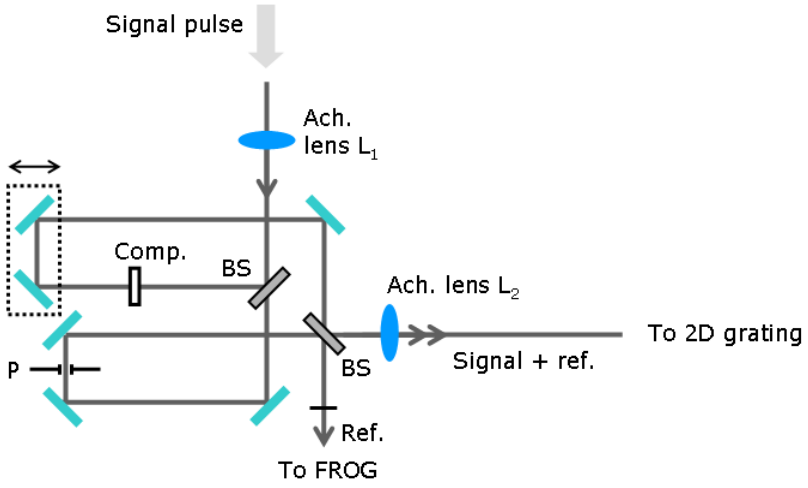

Figure 4.13. Mach-Zehnder interferometer used for a fully self-referenced STRIPED FISH. $\mathbf{L_{1,2}}$: achromatic doublets arranged as a telescope; **P**: 50-µm pinhole in the focal plane of the doublets; **BS**: half-silvered broadband mirror; **Comp**: compensating plate. In this top view, the signal and the reference pulses are displaced vertically and overlap on the drawing. The interferometer is dispersion-compensated over 150 nm.

Figure 4.13 shows an implementation of a fully self-referenced STRIPED FISH. This optical setup is further optimized for broadband light. Note that we place two achromatic doublets with identical focal lengths *outside* the interferometer in order to form a spatial filter in the reference arm with a 50-µm pinhole. While the two lenses can simply be contained within the reference arm of the interferometer, placing them in the common path of the interferometer reduces the effects of dispersion. To further minimize dispersion, a 1-mm fused silica compensating plate is used to cancel the effects of the substrate of the beam-splitter. We also use a half-silvered plate as a beam-splitter to

prevent the higher-order dispersion terms due to multi-layer resonance usually present in dielectric beam-splitters [96].

As a result, this interferometer is dispersion-compensated over a large bandwidth. This is demonstrated by the observation of a STRIPED FISH trace spanning over 150 nm (Figure 4.14). This trace was obtained by measuring a very broadband pulse generated by white-light continuum. An amplified pulse from the chirped-pulse amplifier (~50 μJ, ~200 fs) is focused into a long fused silica window. Because of third-order nonlinear effects, the pulse undergoes self-focusing and self-phase modulation in bulk fused silica [97], resulting in very broadband light that appears white to the eye.

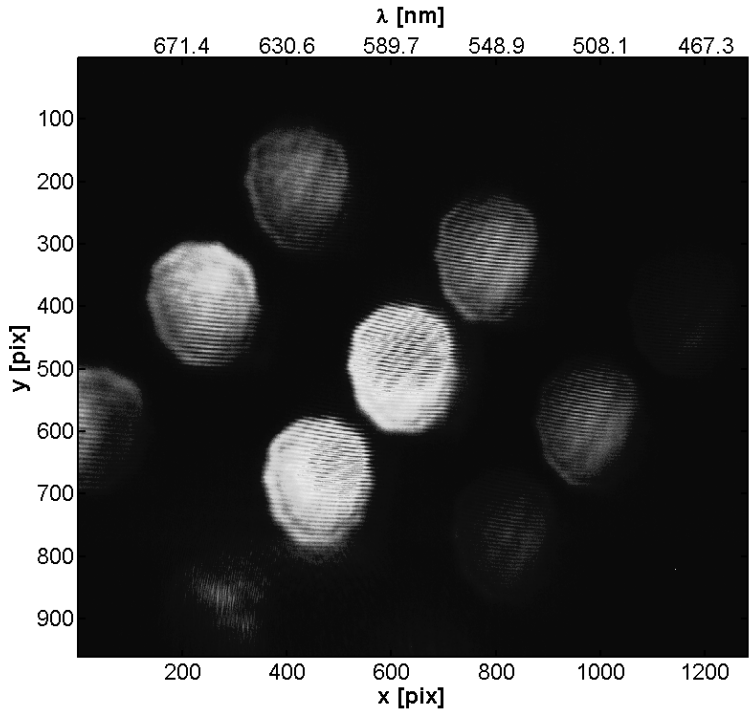

Figure 4.14. STRIPED FISH trace recorded with a fully self-referenced broadband interferometer from white-light continuum in bulk fused silica.

The Mach-Zehnder interferometer results in two (pairs of) outputs. One pair of output beams, composed of the signal and reference pulses is crossed at a small vertical angle α and is directed to the two-dimensional diffraction grating. In the other pair of output beams, the signal pulse is blocked and the reference pulse is sent to a FROG device to measure its spectral phase. The FROG device that is used must match the characteristics (bandwidth, duration, complexity) of the pulse to be measured as well as the desired temporal and spectral resolution. Various FROG devices are available [8], and whenever possible we used a compact single-shot SHG FROG device [80]. Its principle of operation and characteristics are detailed in Appendix A. Once the STRIPED FISH trace is recorded, the complete electric field is then analyzed using the same algorithm as presented in Section 4.3.

4.7 Conclusion and perspectives

Wavelength-multiplexed digital holography allows for the first time to completely characterize (i.e., in intensity and phase and as a function of three dimensions x, y and t) the electric field of a femtosecond laser pulse on a single-shot basis. This method has been experimentally implemented using a simple device (STRIPED FISH) based on only a few key elements, in particular a diffractive beam splitter and a high resolution digital camera. We demonstrated the measurement of spatio-temporal distortions, a chief preoccupation in amplified systems.

The design of our current implementation, however, leaves room from improvement. One drawback, for instance, is the overall low efficiency of the DOE, in particular when a large number of diffracted beams is sought (i.e., $b/a \gg 1$). This poses a

problem for the single-shot measurement of unamplified pulses. One potential solution is to use a DOE with phase (rather than amplitude) modulation; another approach that could be investigated is the "recycling" of the strong undiffracted order that could be used as a reference pulse after appropriate spatial filtering and zero-delay synchronization (a similar idea has been demonstrated in the context of film holograms [98]).

Another area that can benefit from an improved design is the spectral and spatial resolution of the device. The spectral resolution is presently limited by the bandwidth of the stock interference filter. Custom dielectric layers or a high-finesse etalon should be able to considerably improve the spectral resolution of the device. The spatial resolution currently depends on the number of pixels in the digital camera. Although we used a fairly high pixel-count system (>5 megapixels), the resolution of these systems is ever increasing (Dalsa Corp. announced last year that it successfully manufactured a ~10×10-cm chip with over 110 megapixels). With a higher pixel-count, it can be expected that the spatial resolution of a STRIPED FISH device can be substantially increased.

CHAPTER 5

SPATIO-TEMPORAL CORRELATION COEFFICIENTS

The work presented in this chapter originally appeared in the following paper: [99] P. Gabolde, D. Lee, S. Akturk and R. Trebino, *Describing first-order spatio-temporal distortions in ultrashort pulses using normalized parameters*, Optics Express **15** (1) 242-251 (2007).

5.1 Introduction

Ultrashort-pulse lasers are carefully designed to generate the shortest possible pulses, as this is highly desirable in most experimental situations, from micro-machining to multi-photon microscopy [5, 18]. Unfortunately, in propagating through materials, different frequencies ω experience different group delays $\tau(\omega)$, so all transmissive optical components broaden and chirp pulses. Fortunately, pulse compressors can compensate for this group-delay dispersion (GDD) [100]. But, in order to operate, pulse compressors (as well as shapers and stretchers) deliberately rely on an array of *spatio-temporal distortions*, which include angular dispersion, spatial chirp, pulse-front tilt, and angular delay, to name a few. While in theory perfect alignment of a compressor guarantees that the output pulse is free of any of these distortions, in practice residual distortions are often present.

Fortunately, measurement techniques for temporal chirp have been available for decades [8, 21, 80], but convenient diagnostics for most spatio-temporal distortions are just becoming available [9, 71, 72, 101, 102]. As a result, while temporal chirp is well understood, the various spatio-temporal distortions that can occur in ultrashort pulses are not understood as well. Such distortions are as detrimental to experiments as temporal

chirp, especially when the pulse is focused onto a sample [103]. A solid understanding of such distortions is therefore critical, and must begin with a common language with which to discuss them.

Unfortunately, such a language does not currently exist. Consider, for example, the case of spatial chirp. Spatial chirp is a coupling between x and ω and corresponds to a variation of the beam center vs. frequency that can be characterized by the derivative $dx/d\omega$ (called spatial dispersion) to first order. But spatial chirp may equally well be described by a variation in the center frequency vs. position, and hence the derivative $d\omega/dx$ (called frequency gradient), and these two derivatives are not reciprocal [104]. To further complicate matters, some authors use the frequency υ rather than the angular frequency ω [105], while others prefer the wavelength λ. As a result, spatial chirp measurements alone can be reported using *six different* derivatives, all with different units. Worse, it is difficult to estimate the *severity* of spatial chirp from any of these quantities, and how much – or how little – it may eventually affect the performance of an ultrafast system. The cases of pulse-front tilt, angular dispersion, and angular delay are similar. They can be described, respectively, by the derivatives dt/dx, $dk_x/d\omega$, and dk_x/dt. Or they can be described by the several additional analogous definitions. Thus studies of other spatio-temporal distortions suffer from the same problems.

In this chapter we propose an intuitive formalism to describe spatio-temporal distortions. Rather than using first-order derivatives, we rely on normalized correlation parameters that were introduced in the context of perfect Gaussian pulses and beams [27]. We also show that such normalized parameters are well adapted to experimental

situations where the spatio-temporal distortions of pulses and beams of arbitrary profiles must be minimized in real time.

5.2 Definition of spatial chirp and other spatio-temporal couplings

We begin by recalling the formal definitions of the above-mentioned normalized spatio-temporal couplings parameters. We first consider (horizontal) spatial chirp, a coupling in the x–ω domain. Generalization to the other spatio-temporal couplings, namely pulse-front tilt, angular dispersion, and angular delay, is immediate by considering the x–t, k_x–ω and k_x–t domains. Extension to the y coordinate is also immediate.

We call $I(x,\omega) \equiv |E(x,\omega)|^2$ the (spatio-spectral) intensity distribution of the pulse, where x and ω are measured with respect to the beam center and the carrier frequency (that is, have the mean position and mean frequency subtracted off). The intensity $I(x,\omega)$ is normalized such that its integral over space and frequency is 1. We now define the normalized spatial chirp parameter $\rho_{x\omega}$ as the first mixed moment of $I(x,\omega)$, divided by the global beam size Δx and the global bandwidth $\Delta\omega$:

$$\begin{aligned} \rho_{x\omega} &\equiv \frac{\iint dx\, d\omega\, I(x,\omega)\, x\omega}{\Delta x \Delta\omega} \\ \text{where } \Delta x &\equiv \left[\iint dx d\omega I(x,\omega) x^2 \right]^{1/2} \\ \text{and } \Delta\omega &\equiv \left[\iint dx d\omega I(x,\omega) \omega^2 \right]^{1/2} \end{aligned} \tag{5.1}$$

Analogous quantities can be defined for the other first-order spatio-temporal distortions (see Section 5.5).

This definition of spatial chirp as a linear correlation coefficient is applicable to pulses of arbitrary profiles [106], and is consistent with the frequency gradient dω/dx and spatial dispersion dx/dω parameters introduced in Ref. [27] for Gaussian pulses, in the sense that:

$$\rho_{x\omega} = \frac{\Delta x}{\Delta \omega}\frac{d\omega}{dx} = \frac{\Delta \omega}{\Delta x}\frac{dx}{d\omega} \tag{5.2}$$

Note that since $\rho_{x\omega}$ is calculated from $|E(x,\omega)|^2$, it does not include a coupling between x and ω that may appear in the *phase* of $E(x,\omega)$. This coupling essentially amounts to angular dispersion [27], and is treated in Section 5.5.

There are numerous properties of this correlation coefficient that make it an attractive choice from a practical point of view:

● It is an extension to arbitrary pulses and beams that is consistent with previous definitions of frequency gradient and spatial dispersion.

● It is symmetric: when $I(x,\omega)$ is recorded using a camera, it does not matter whether the position axis is vertical and the frequency axis horizontal, or vice-versa.

● It is scale-invariant: except for a possible change of sign, it is unaffected by the transformations $x \rightarrow \alpha x$ or $\omega \rightarrow \beta\omega$. Thus, beam magnification does not affect the result. An important practical implication is that experimental trace need not be calibrated: the variables x and ω can represent pixel numbers on a camera, and not necessarily physical quantities with proper units.

● It is a dimensionless number.

● Because $\rho_{x\omega}$ can be identified with the linear correlation of the joint distribution $I(x,\omega)$ [106], it is even possible to show that:

$$-1 < \rho_{x\omega} < 1. \tag{5.3}$$

● Conveniently, $\rho_{x\omega} = 0$ corresponds to the absence of the distortion to first order, while an increased value of $|\rho_{x\omega}|$ indicates an increase in the magnitude of spatial chirp (see Figure 5.1).

● The sign of $\rho_{x\omega}$ simply reveals whether the beam center position increases or decreases with ω.

● Also, for all but near-single-cycle pulses, the change from frequency ω to wavelength λ is a linear transformation: $\lambda = -\lambda_0^2\omega/(2\pi c)$; again, λ is measured with respect to the central wavelength λ_0. Written in this form, the change from ω (or υ) to λ is just a change of scale and sign, and therefore:

$$\rho_{x\lambda} = -\rho_{x\nu} = -\rho_{x\omega} \tag{5.4}$$

● Finally, $\rho_{x\omega}$ is equal to the *eccentricity* of an elliptical beam caused by spatial chirp.

To see that the last statement is true, consider a collimated beam with an initial circular beam profile going through an optical device that introduces spatial chirp in the x direction (for example, a misaligned stretcher). We take the input beam to have the same size in the x and y directions: $\Delta x = \Delta y$. Because of spatial chirp, the size of the output beam in the x direction increases to $\Delta x'$. The output beam is therefore elliptical, and can be characterized by its eccentricity e_{xy}:

$$e_{xy} = \sqrt{1 - \frac{\Delta y^2}{\Delta x'^2}} = \sqrt{1 - \frac{\Delta x^2}{\Delta x'^2}}, \quad 0 \le e_{xy} < 1 \tag{5.5}$$

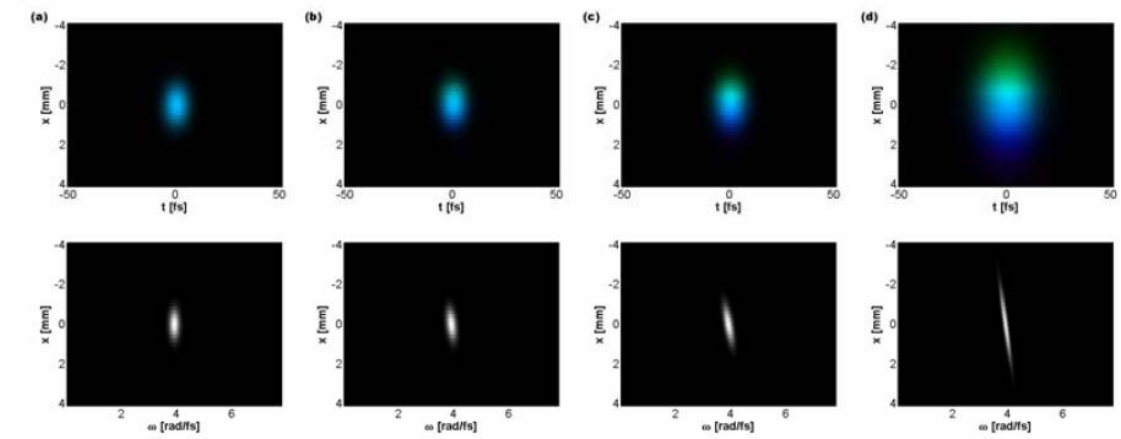

Figure 5.1. Profiles of an ultrashort pulse with increasing amounts of spatial chirp, and hence with increasing values of $\rho_{x\omega}$. Upper row: spatio-temporal profiles. The pulses have a central wavelength of 480 nm, and 35 nm of bandwidth. Lower row: corresponding profiles of $I(x,\omega)$, from which $\rho_{x\omega}$ is calculated. **(a)** $\rho_{x\omega} = 0.00$. **(b)** $\rho_{x\omega} = 0.30$. **(c)** $\rho_{x\omega} = 0.60$. **(d)** $\rho_{x\omega} = 0.90$.

Comparing Equation (5.5) with Equation (45) in Ref. [27], we see that $|\rho_{x\omega}| = e_{xy}$. Although it is easy and intuitive to *think* of $\rho_{x\omega}$ in terms of the eccentricity of the spatial profile, for precise measurements it is preferable to rely on $\rho_{x\omega}$ obtained from the intensity distribution $I(x,\omega)$. In addition, note that if spatial chirp results in a spatial broadening of the beam, and therefore in an elliptical beam, it also results in a *temporal* broadening of the pulse, because of the decrease of available bandwidth at each point x in the beam. Thus, in the presence of spatial chirp, the duration of a pulse with a flat spectral phase does *not* reach its Fourier limit, as can be clearly seen on Figure 5.1(d).

As a side note we would like to point out that the correlation parameter $\rho_{x\omega}$ – and more generally any correlation coefficient ρ that appears in this chapter – is very sensitive to small amounts of spatio-temporal coupling, but saturates to a near-unity value for extremely large amounts of coupling (this situation is explored in more details in Section 5.5).

5.3 Experimental measurements

We now present a simple arrangement (Figure 5.2) that we used to measure the intensity distributions $I(x,\lambda)$ and $I(y,\lambda)$, and we show how to calculate $\rho_{x\lambda}$ and $\rho_{y\lambda}$ from experimental data.

The beam under test is first dispersed in the horizontal plane by a diffraction grating G_1, and the diffracted order $m_1 = 1$, focused by a cylindrical lens, illuminates a digital camera. Simultaneously, the specular reflection ($m_1 = 0$) from G_1 is sent onto a second grating G_2 that disperses the beam *vertically* in a Littrow configuration so that all the beams of interest are contained in the same horizontal plane; the first order ($m_2 = -1$) of G_2 is focused by a second cylindrical lens and illuminates the same digital camera. By blocking the order $m_1 = 1$ from G_1, the camera records $I(x,\lambda)$, while by blocking the order $m_1 = 0$, the camera records $I(y,\lambda)$.

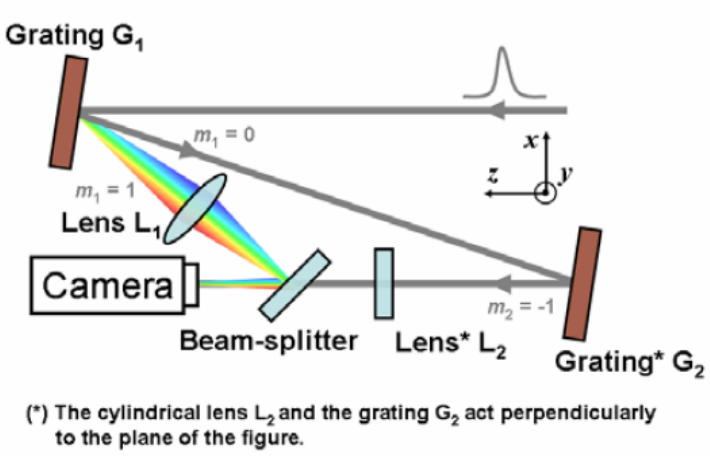

Figure 5.2. Apparatus used to record $I(x,\lambda)$ and I(y,λ). $\mathbf{G_1}$ diffraction grating (dispersing in plane); $\mathbf{L_1}$ cylindrical lens (collimating in plane); $\mathbf{G_2}$ diffraction grating (in Littrow, dispersing out of plane); $\mathbf{L_2}$ cylindrical lens (collimating out of plane).

Once the two images have been recorded, extracting the parameter $\rho_{x\lambda}$ and $\rho_{y\lambda}$ from $I(x,\lambda)$ and $I(y,\lambda)$ is a direct application of Equation (5.1), as long as the integrals are replaced by discrete sums. As stated in Section 5.2, it is not necessary to calibrate the axes of the digital camera: x, y and λ can simply refer to pixel numbers. Additionally, we use the fact that the wavelength axis can be either horizontal or vertical. However, Equation (5.1) does require that the function $I(x,\lambda)$ be centered with respect to its axes. When pixel numbers are used, this is never the case, and therefore it is easier to rewrite Equation (5.1) in the case of un-centered, discrete distributions. To do so, we first introduce the moments μ_{pq} of the intensity distribution $I(x,\lambda)$:

$$\mu_{pq} \equiv \sum_{x,\lambda} I(x,\lambda) x^p \lambda^q \tag{5.6}$$

The spatial chirp parameter $\rho_{x\lambda}$ is then computed using the following equation, which is a convenient form of Equation (5.1) that does not require the data $I(x,\lambda)$ to be centered:

$$\rho_{x\lambda} = \frac{\mu_{11} - \mu_{01}\mu_{10}}{\left[\mu_{20} - {\mu_{10}}^2\right]^{1/2}\left[\mu_{02} - {\mu_{01}}^2\right]^{1/2}} \tag{5.7}$$

Note that some devices are able to detect spatial chirp without the complete measurement of $I(x,\lambda)$ [9]. In that case the spatial chirp parameter $\rho_{x\lambda}$ may be calculated using Equation (5.2) instead.

Because Equation (5.7) involves sums on the entire image, it is likely to include various background effects, such as scattered light or thermal noise, that might affect the recorded image, in particular in regions where the intensity $I(x,\lambda)$ is low. To mitigate these effects, it is desirable to apply a threshold to $I(x,\lambda)$ before calculating $\rho_{x\lambda}$, by setting to 1 any values of the intensity that are above a pre-defined threshold, and setting the others to 0 (see Figure 5.3 for an example). As a simple alternative, it is possible to let the camera saturate a large portion of the trace, and only retain the saturated values (i.e., setting non-saturated values to zero) before applying Equation (5.7). We found both methods to be consistent and equivalently robust to noise, and numerical simulations show that they yield the same result as a direct application of Equation (5.7).

In summary, Equation (5.6) and (5.7) provide a simple, efficient and robust method to calculate $\rho_{x\lambda}$. This procedure is extremely well adapted to data-processing computer programs like MATLAB, and allows easy monitoring of the spatial chirp in real time during the alignment of complex ultrafast laser systems.

5.4 Experimental results

We applied this method to monitor spatial chirp as we aligned a mode-locked Ti:sapphire laser with an external pulse compressor seeding a chirped-pulse amplifier (Quantronix RGA 4800). The apparatus was set up as described above, and images were captured by a 1024×728 Firewire digital camera (Sony XCD-710) directly in MATLAB where the parameters $\rho_{x\lambda}$ and $\rho_{y\lambda}$ were calculated and displayed in real time.

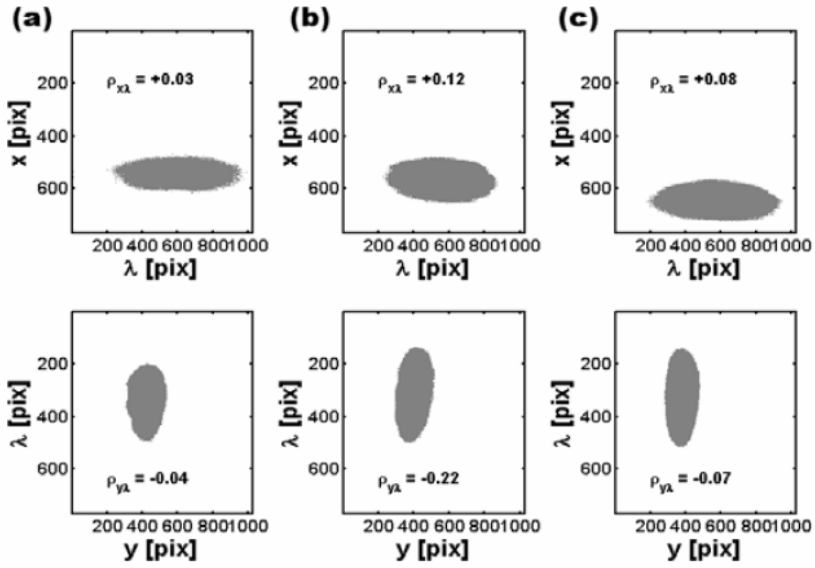

Figure 5.3. Typical raw experimental data obtained during real-time monitoring of a Ti:sapphire oscillator and its external prism pulse compressor, showing the parameters $\rho_{x\lambda}$ (top row) and $\rho_{y\lambda}$ (bottom row) obtained after applying a threshold on the measured images. **(a)** Oscillator output before the external pulse compressor. **(b)** External pulse compressor output, misaligned in the vertical plane. **(c)** External pulse compressor output, adjusted in the vertical plane.

We should point out that in this study we chose to monitor spatial chirp as an example; of course, it is well known that spatio-temporal distortions from a stretcher or a compressor arise from residual angular dispersion [51]. However, as the pulse emerging

from these devices propagates in free space, angular dispersion results in spatial chirp, and minimizing spatial chirp in the far field amounts to minimizing residual angular dispersion.

To ensure a proper alignment of the gratings and cylindrical lenses in the setup, we used a reference pulse that was spatially filtered using a single-mode fiber. We then monitored the values of spatial chirp along x and y as we aligned the system (Figure 5.3). Table 5.1 shows typical values of spatial chirp that we found during this procedure. A misaligned stretcher exhibits typical values of ρ = 0.50–0.60, and occasionally values as high as 0.80 or 0.90. Realignment of a retro-reflector inside the unit brought ρ to values typically below 0.20. Even smaller values are obtained after amplification and re-compression, which we attribute to the spectral clipping that happens in our compressor unit. During these alignment procedures, beam pointing changes resulted in deviations of $\rho_{x\lambda}$ on the order of 0.01, which can be roughly considered as the experimental detection limit of our setup.

Table 5.1. Typical values of spatial chirp measured in different ultrafast optical systems.

Laser system	$\lvert\rho_{x\lambda}\rvert$	$\lvert\rho_{y\lambda}\rvert$
Ti:sapphire oscillator (spatially filtered)	<0.01	<0.01
Ti:sapphire oscillator	<0.05	<0.05
Ti:sapphire oscillator (with an external pulse compressor)	0.05–0.10	0.05–0.10
Misaligned pulse stretcher in a CPA	0.20–0.50	~0.60
Realigned pulse stretcher in a CPA	0.20	<0.01
CPA output pulse (stretched, amplified, recompressed)	0.05–0.20	0.05–0.20

5.5 Analogy with pulse broadening and extension to other distortions

There is a perfect analogy between the effects due to dispersion, and those due to spatio-temporal distortions. The first-order cause of pulse broadening due to dispersion is often characterized by the group-delay dispersion, $d\tau/d\omega$, although this can also be considered as a temporal variation of the instantaneous frequency ω_{inst} at a constant rate $d\omega_{inst}/dt$. In analogy with Equation (5.2), it is possible to define a temporal chirp parameter $\rho_{\omega t}$, normalized by the pulse duration Δt and the bandwidth $\Delta\omega$, and that satisfies:

$$\rho_{\omega t} = \frac{\Delta t}{\Delta \omega}\frac{d\omega_{inst}}{dt} = \frac{\Delta \omega}{\Delta t}\frac{d\tau}{d\omega} \tag{5.8}$$

The temporal chirp parameter $\rho_{\omega t}$ can also be defined in a form similar to Equation (5.1) by considering the Wigner distribution of the pulse $I_W(\omega,t)$. As an example, consider a chirped Gaussian pulse with a bandwidth $\Delta\omega$ and a group-delay dispersion $d\tau/d\omega$:

$$E(\omega) = E_0 \exp\left[-\frac{\omega^2}{4\Delta\omega^2} + \frac{i}{2}\frac{d\tau}{d\omega}\omega^2\right] \tag{5.9}$$

The Wigner distribution of this pulse is given by [48]:

$$I_W(\omega,t) \propto \left|E_0\right|^2 \exp\left[-\frac{\omega^2}{2\Delta\omega^2} - \frac{\left(t-\left(d\tau/d\omega\right)\omega\right)^2}{1/\left(2\Delta\omega^2\right)}\right] \tag{5.10}$$

Note the presence of the coupling term $t - (d\tau/d\omega)\omega$, whose ω-dependent term becomes important when $d\tau/d\omega \neq 0$ (i.e., $\rho_{\omega t} \neq 0$), and which is similar to the coupling term, $x - (dx/d\omega)\omega$, that arises in the case of spatial chirp ($\rho_{x\omega} \neq 0$).

It is very instructive to consider the relation between $\rho_{\omega t}$ and the pulse duration Δt because dispersion effects are easily and intuitively interpreted in the time domain. Figure 5.4 shows the dependence of the pulse duration (normalized to its Fourier limit) with $\rho_{\omega t}$. It is obvious that the parameter $\rho_{\omega t}$ is very sensitive to *small amounts of dispersion*: a value of $\rho_{\omega t} = 0.30$ corresponds to a pulse stretched by only 5%, which is acceptable in many situations. On the other hand, very large stretching ratios, such as those obtained by pulse stretchers in CPA systems, correspond to values of $\rho_{\omega t}$ very close to 1, and rapidly become indistinguishable. Thus, these correlation coefficients are ideal for monitoring ultrafast systems that must approach the Fourier limit, but less than ideal for cases in which one is deliberately attempting to introduce massive amounts of these distortions.

In this respect, it is also interesting to compare the normalized parameters that we introduce here with another normalized parameter that was proposed for the study of spatio-temporal distortions in general: the *degree of spatio-temporal uniformity* μ [71]. This parameter is calculated from the spatially and spectrally resolved electric field *amplitude*:

$$\mu \equiv \frac{\iint d\omega_1 d\omega_2 \left| \int dx\, E(x,\omega_1) E^*(x,\omega_2) \right|^2}{\left[\iint dx\, d\omega \left| E(x,\omega) \right|^2 \right]^2} \tag{5.11}$$

The degree of spatio-temporal uniformity μ may be measured experimentally using linear techniques, and it describes *all* possible spatio-temporal couplings, which can be convenient in some cases: $\mu = 1$ corresponds to a pulse free of spatio-temporal distortions, while $0 < \mu < 1$ indicates that some distortions are present. However, the parameter μ is not very sensitive to small amounts of spatio-temporal distortions. As shown in Figure 5.5 in the case of spatial chirp, there is little change in μ in the region of small distortions ($\rho_{x\omega} \simeq 0$).

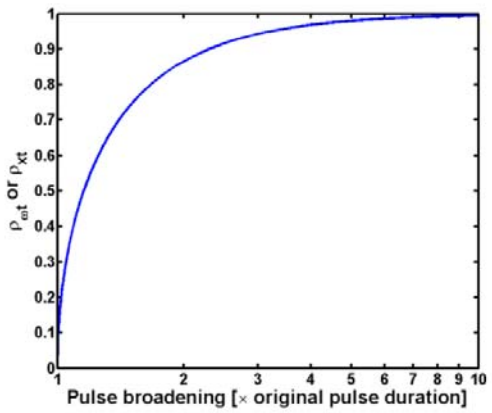

Figure 5.4. Normalized temporal chirp parameter $\rho_{\omega t}$ as a function of pulse broadening. Because pulse-front tilt also results in pulse broadening, this curve can also represent ρ_{xt}, as well as $\rho_{x\omega}$ if pulse broadening is replaced by beam magnification along x.

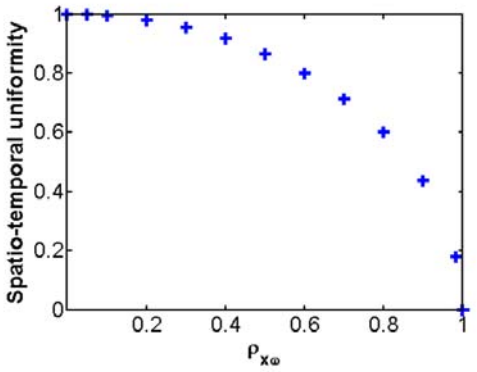

Figure 5.5. Numerical simulations of the degree of spatio-temporal uniformity μ as a function of the spatial chirp parameter $\rho_{x\omega}$ in the case of a Gaussian beam.

Due to the analogy between spatial and temporal chirp, it seems logical to impose equivalent tolerances on $\rho_{\omega t}$ and $\rho_{x\omega}$. In practice, $|\rho| \leq 0.30$ or 0.40 seems a reasonable condition to aim for. These considerations are also valid for the parameters ρ_{xt}, $\rho_{k\omega}$ and ρ_{kt}, which can be used to measure pulse-front tilt, angular dispersion, and angular delay, respectively, as long as the intensity distributions $I(x,t)$, $I(k_x,\omega)$ and $I(k_x,t)$ are known:

$$\rho_{xt} \equiv \frac{\iint dxdtI(x,t)xt}{\Delta x \Delta t} \text{ (pulse-front tilt)}$$
$$\rho_{k\omega} \equiv \frac{\iint dkd\omega I(k_x,\omega)k_x\omega}{\Delta k_x \Delta \omega} \text{ (angular dispersion)} \qquad (5.12)$$
$$\rho_{kt} \equiv \frac{\iint dkdtI(k_x,t)k_x t}{\Delta k_x \Delta t} \text{ (angular delay)}$$

At least to some extent, all of these spatio-temporal distortions are present at the same time in real pulses. It is an experimental challenge to control all these distortions, especially considering the fact that they are often entangled. Pulse-front tilt, for example, can be caused by angular dispersion [107] or simultaneous spatial and temporal chirp

[108]. In the latter scenario, it is possible to derive an exact expression for pulse-front tilt in the ideal case of Gaussian pulses and beams: $dt/dx = (d\tau/d\omega)\times(d\omega/dx)$. This formula can be expressed in terms of normalized ρ-parameters as well: $\rho_{xt} = \rho_{x\omega}\times\rho_{\omega t}$ (see Figure 5.6 for an example). For more complex pulses however, closed-form expressions for relationships between spatio-temporal distortions become difficult to establish, and from a practical point of view it is preferable to aim at maintaining all the various ρ-parameters below a certain threshold (e.g., 0.30) that eventually depends on the overall spatio-temporal pulse quality that is sought.

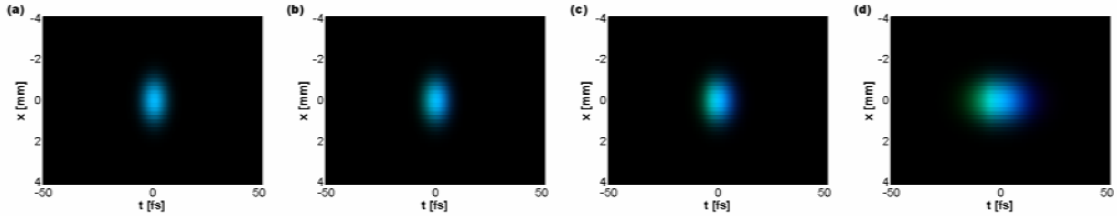

Figure 5.6. Temporal profiles of an ultrashort pulse with increasing amounts of positive temporal chirp, and hence with increasing values of $\rho_{\omega t}$. The pulses have a central wavelength of 480 nm, and 35 nm of bandwidth. **(a)** $\rho_{\omega t}$ = 0.00 (transform limit). **(b)** $\rho_{\omega t}$ = 0.30 (5% broadening). **(c)** $\rho_{\omega t}$ = 0.60 (25% broadening). **(d)** $\rho_{\omega t}$ = 0.90 (130% broadening).

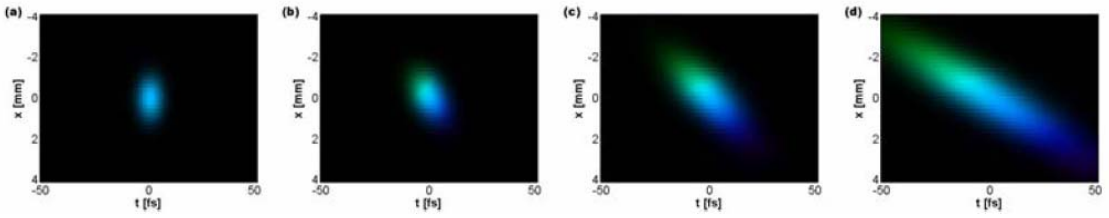

Figure 5.7. Spatio-temporal profiles of an ultrashort pulse with increasing amounts of temporal and spatial chirp, and hence with increasing values of ρ_{xt}. The pulses have a central wavelength of 480 nm, and 35 nm of bandwidth. **(a)** ρ_{xt} = 0.00. **(b)** ρ_{xt} = 0.30. **(c)** ρ_{xt} = 0.60. **(d)** ρ_{xt} = 0.80.

5.6 Conclusion and perspectives

We have presented an intuitive description of various spatio-temporal distortions in terms of a set of normalized correlation coefficients. Spatial chirp, pulse-front tilt, angular dispersion and angular delay, and also temporal chirp, can all be described to first order by dimensionless parameters that vary in the range [-1,1] and readily indicate the *severity* of these distortions. These parameters are especially sensitive to small amounts of distortion. We also presented a simple, practical apparatus allowing the real-time monitoring of the corresponding spatial-chirp parameters $\rho_{x\lambda}$ and $\rho_{y\lambda}$. We believe that these parameters will help better understand spatio-temporal distortions and their consequences, and will be used as a benchmark enabling the comparison of the performance of ultrafast lasers.

One obvious restriction of the description of the spatio-temporal distortions presented in this chapter is that all these distortions are considered at a fixed plane along the optical axis. While it seems intuitive that some distortions (e.g., angular dispersion) should remain unaffected by free-space propagation, it is obvious that others (e.g., spatial chirp) can evolve as a short pulse propagates. Indeed, angular dispersion can be regarded as the *source* of spatial chirp.

As an example, Figure 5.8 shows a numerical simulation of the build up of spatial chirp along the direction of propagation of a beam with angular dispersion at $z = 0$. Such preliminary simulations suggest that the characteristic distance with which spatial chirp appears in the beam scales as $\rho_{k\omega}^{-1/2}$. Further work is needed to confirm such a trend and

to generalize it to the other spatio-temporal distortions (pulse-front tilt and angular delay), especially in the presence of temporal dispersion.

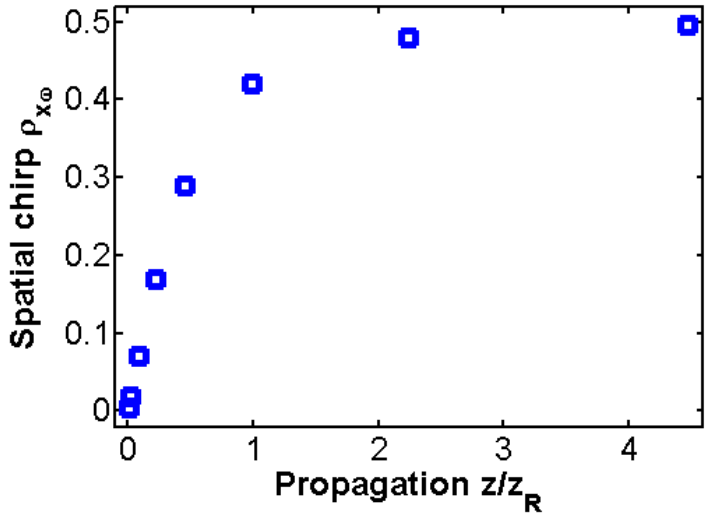

Figure 5.8. Numerical simulation of the increase of spatial chirp $\rho_{x\omega}$ with free-space propagation for a Gaussian beam of Rayleigh range z_R and initial angular dispersion $\rho_{k\omega} = 0.50$ at $z = 0$.

Another possible extension of the work presented in this chapter is a definition and study of normalized spatio-temporal distortion parameters in the case of higher-order distortions. Indeed, the ρ-parameters also seem to offer the possibility to describe spatio-temporal distortions beyond the first order, such as chromatic aberrations in lenses, or pulse-front curvature, by considering higher-order cross moments μ_{pq} of the relevant intensity distributions. Including spectral or temporal phase terms beyond the second order would also greatly extend the range of application of any theory of spatio-temporal distortions.

APPENDIX A

FREQUENCY-RESOVED OPTICAL GATING

In this appendix, we describe frequency-resolved optical gating (FROG), the standard technique that we use to obtain the temporal (or spectral) intensity and phase of femtosecond pulses, notably the reference pulses that are used in many experiments presented in this study. FROG is an extension of the intensity autocorrelation that can be implemented experimentally as a compact single-shot device.

A.1 Intensity autocorrelation of femtosecond pulses

Among the first attempts to measure the temporal shape of femtosecond pulses is the use of the intensity autocorrelation. The pulse under test, $E(t)$, is mixed in a doubling nonlinear crystal with a delayed replica, $E(t-\tau)$, to obtain the signal field $E(t)E(t-\tau)$. For pulses with a center wavelength of $\lambda_0 = 800$ nm, the nonlinear crystal of choice is often BBO (β-barium borate) because of its extended transparency and phase-matching properties down to ~200 nm, its large nonlinear coefficients and high damage threshold [109]. Figure A.1 shows a typical intensity autocorrelation setup.

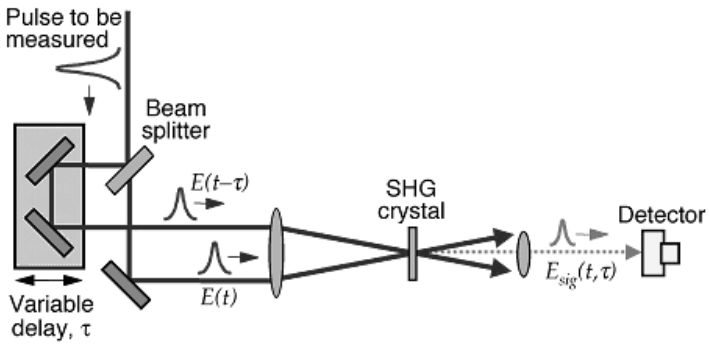

Figure A.1. Setup to measure the non-collinear second-harmonic background-free intensity autocorrelation.

To record the intensity autocorrelation, the delay τ between the two replica of the pulses is scanned while the intensity of the sum-frequency signal, $I(t)\mathrm{I}(t-\tau)$, is recorded at the second harmonic (~400 nm) with a slow detector to yield the "background-free" intensity autocorrelation [21]:

$$A(\tau) = \int_{-\infty}^{+\infty} I(t)I(t-\tau)dt \tag{A.1}$$

Obviously, the intensity autocorrelation function, $A(\tau)$, must contain information regarding the input pulse duration, Δt, since it must be maximum at $\tau = 0$ and must vanish for $\tau \gg \Delta t$. Indeed, the root-mean-square (rms) width of the intensity autocorrelation is simply $\sqrt{2}$ times the rms width of the pulse intensity duration [22, 110]. The intensity autocorrelation therefore gives a good estimate of the pulse duration, but Equation (A.1) clearly shows that it is insensitive to the (temporal) *phase* of the pulse under test.

A.2 Spectrally-resolved intensity autocorrelation

To overcome the limitations of the intensity autocorrelation, various schemes have been proposed and implemented [21, 34, 111-113]. Among them, one is a simple extension of the intensity autocorrelation: FROG is just a spectrally-resolved intensity autocorrelation. To measure a FROG "trace" one merely replaces the photo-detector used to measure the intensity autocorrelation by a spectrometer that resolves in frequency the signal field generated in the nonlinear crystal. Mathematically, the FROG trace is therefore a two-dimensional function of delay τ and frequency ω:

$$I_{FROG}(\omega,\tau) = \left| \int_{-\infty}^{+\infty} E(t)E(t-\tau)e^{-i\omega t}dt \right|^2 \tag{A.2}$$

Unlike Equation (A.1), Equation (A.2) depends on the temporal phase of the input electric field. However, a closed-form inversion of Equation (A.2) is not possible, and instead an iterative algorithm is used to find the electric field $E(t)$ whose FROG trace best matches the recorded experimental trace [113]. A typical FROG setup is pictured on Figure A.2. In this case two pulses are crossed in a doubling crystal to generate a sum-frequency signal, but other geometries are possible depending on the experimental situation [8].

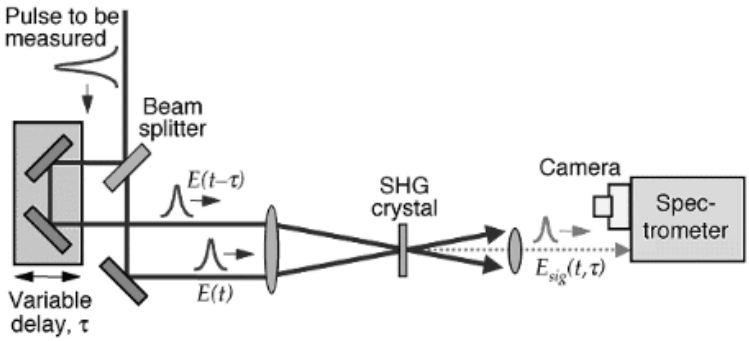

Figure A.2. Setup to measure the non-collinear second-harmonic FROG trace.

A.3 Single-shot geometry

The setup pictured in Figure A.2 requires a mechanical scan of a delay line to record the two-dimensional FROG trace. This requires a fine optical alignment of the various elements and prevents a single-shot operation of the device. To overcome these limitations, compact single-shot FROG devices have been developed. The beam-splitter and delay line are replaced by a Fresnel bi-prism so that two beams cross within the nonlinear crystal that is imaged onto a detector [80, 114]. The device is further simplified by using a long nonlinear crystal to decrease its phase-matching bandwidth so that the sum-frequency signal that is generated in the crystal is angularly dispersed according to the phase-matching angle [80]. Figure A.3 depicts how a delay-scanning second-harmonic FROG setup can be converted to a single-shot geometry.

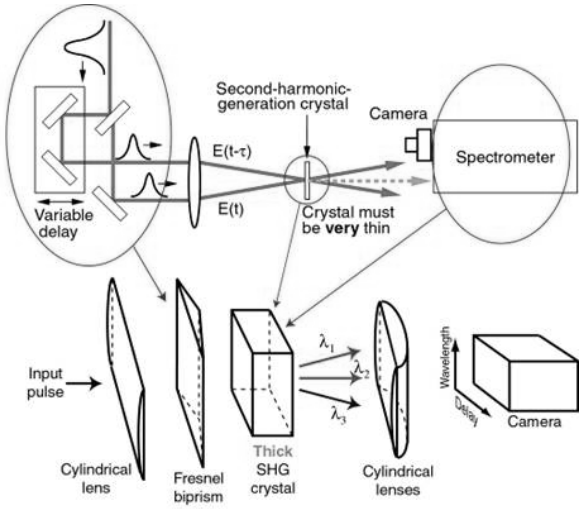

Figure A.3. Delay-scanning second-harmonic-generation FROG setup **(top)** replaced by an equivalent single-shot geometry **(bottom)**.

In this single-shot geometry, FROG traces are recorded using a two-dimensional digital camera. The same iterative algorithm can be used as for delay-scanning FROG to retrieve the electric field of the input pulse, $E(t)$. The range of pulses that can be measured with a given device is mainly determined by the crystal and the geometry that are used. Table A.1 lists the characteristics of the devices we have used in this study to measure the temporal (and spectral) dependence of the reference pulses.

Table A.1. Characteristics of the single-shot FROG devices used in this study.

Model number	8−20	8−50	15−100
Laser wavelength	800 nm	800 nm	1.5 μm
Pulse duration range	20−200 fs	50−500 fs	100−1000 fs
Max. spectral content	160 nm	50 nm	60 nm
Spectral resolution	4 nm	2 nm	1.7 nm

REFERENCES

[1] P. F. Moulton, "Spectroscopic and laser characteristics of Ti:Al2O3," J. Opt. Soc. Am. B **3**, 125-133 (1986).

[2] T. Fuji, A. Unterhuber, V. S. Yakovlev, G. Tempea, A. Stingl, F. Krausz, and W. Drexler, "Generation of smooth, ultra-broadband spectra directly from a prism-less Ti:sapphire laser," Applied Physics B (Lasers and Optics) **77**, 125-128 (2003).

[3] P. A. Franken, A. E. Hill, C. W. Peters, and G. Weinreich, "Generation of optical harmonics," Phys. Rev. Lett. **7**, 118-119 (1961).

[4] J. A. Armstrong, N. Bloembergen, J. Ducuing, and P. S. Pershan, "Interactions between Light Waves in a Nonlinear Dielectric," Phys. Rev. **127**, 1918-1939 (1962).

[5] W. Denk, J. H. Strickler, and W. W. Webb, "Two-Photon Laser Scanning Fluorescence Microscopy," Science **248**, 73-76 (1990).

[6] M. Aoyama, K. Yamakawa, Y. Akahane, J. Ma, N. Inoue, H. Ueda, and H. Kiriyama, "0.85-PW, 33-fs Ti:sapphire laser," Opt. Lett. **28**, 1594-1596 (2003).

[7] J. A. Armstrong, "Measurement of picosecond laser pulse widths," Appl. Phys. Lett. **10**, 16-18 (1967).

[8] R. Trebino, K. W. DeLong, D. N. Fittinghoff, J. N. Sweetser, M. A. Krumbuegel, and D. J. Kane, "Measuring Ultrashort Laser Pulses in the Time-Frequency Domain Using Frequency-Resolved Optical Gating," Rev. Sci. Instrum. **38**, 3277-3295 (1997).

[9] S. Akturk, M. Kimmel, P. O'Shea, and R. Trebino, "Measuring spatial chirp in ultrashort pulses using single-shot Frequency-Resolved Optical Gating," Opt. Express **11**, 68-78 (2003).

[10] E. P. Ippen, C. V. Shank, and A. Dienes, "Passive mode locking of the cw dye laser," Appl. Phys. Lett. **21**, 348-350 (1972).

[11] U. Keller, D. A. B. Miller, G. D. Boyd, T. H. Chiu, J. F. Ferguson, and M. T. Asom, "Solid-state low-loss intracavity saturable absorber for Nd:YLF lasers: an antiresonant semiconductor Fabry-Perot saturable asborber," Opt. Lett. **17**, 505-507 (1992).

[12] T. Brabec, C. Spielmann, P. F. Curley, and F. Krausz, "Kerr lens mode locking," Opt. Lett. **17**, 1292-1294 (1992).

[13] D. E. Spence, P. N. Kean, and W. Sibbett, "60-fsec pulse generation from a self-mode-locked Ti:sapphire laser," Opt. Lett. **16**, 42-44 (1991).

[14] E. B. Treacy, "Optical Pulse Compression With Diffraction Gratings," IEEE J. Quantum Electron. **5**, 454-458 (1969).

[15] R. Szipöcs, K. Ferencz, C. Spielmann, and F. Krausz, "Chirped multilayer coatings for broadband dispersion control in femtosecond lasers," Opt. Lett. **19**, 201-203 (1994).

[16] H. W. Kogelnik, E. P. Ippen, A. Dienes, and C. V. Shank, "Astigmatically Compensated Cavities for CW Dye Lasers," IEEE J. Quantum Electron. **8**, 373-379 (1972).

[17] D. Strickland, and G. Mourou, "Compression of amplified chirped optical pulses," Opt. Commun. **56**, 219-221 (1985).

[18] C. B. Schaffer, A. Brodeur, J. F. García, and E. Mazur, "Micromachining bulk glass by use of femtosecond laser pulses with nanojoule energy," Opt. Lett. **26**, 93-95 (2001).

[19] A. Migus, A. Antonetti, J. Etchepare, D. Hulin, and A. Orszag, "Femtosecond spectroscopy with high-power tunable optical pulses," J. Opt. Soc. Am. B **2**, 584-594 (1985).

[20] W. S. Warren, H. Rabitz, and M. Dahleh, "Coherent Control of Quantum Dynamics: The Dream Is Alive," Science **259**, 1581-1589 (1993).

[21] J.-C. M. Diels, J. J. Fontaine, I. C. McMichael, and F. Simoni, "Control and measurement of ultrashort pulse shapes (in amplitude and phase) with femtosecond accuracy," Appl. Opt. **24**, 1270-1282 (1985).

[22] R. Trebino, *Frequency-Resolved Optical Gating: The Measurement of Ultrashort Laser Pulses* (Kluwer Academic Publishers, 2000).

[23] B. C. Platt, and R. Shack, "History and Principles of Shack-Hartmann Wavefront Sensing," J. Refractive Surg. **17**, S573-S577 (2001).

[24] R. G. Lane, and M. Tallon, "Wave-front reconstruction using a Shack-Hartmann sensor," Appl. Opt. **31**, 6902-6908 (1992).

[25] C. Elster, and I. Weingartner, "Solution to the shearing problem," Appl. Opt. **38**, 5024-5031 (1999).

[26] J.-C. Chanteloup, "Multiple-wave lateral shearing interferometry for wave-front sensing," Appl. Opt. **44**, 1559-1571 (2005).

[27] S. Akturk, X. Gu, P. Gabolde, and R. Trebino, "The general theory of first-order spatio-temporal distortions of Gaussian pulses and beams," Opt. Express **13**, 8642-8661 (2005).

[28] W. Amir, T. A. Planchon, C. G. Durfee, and J. A. Squier, "Simultaneous visualization of spatial and chromatic aberrations by two-dimensional Fourier transform spectral interferometry," Opt. Lett. **31**, 2927-2929 (2006).

[29] P. Bowlan, P. Gabolde, A. Shreenath, K. McGresham, and R. Trebino, "Crossed-beam spectral interferometry: a simple, high-spectral-resolution method for completely characterizing complex ultrashort pulses in real time," Opt. Express **14**, 11892-11900 (2006).

[30] L. Lepetit, G. Chériaux, and M. Joffre, "Linear techniques of phase measurement by femtosecond spectral inteferometry for applications in spectroscopy," J. Opt. Soc. Am. B **12**, 2467-2474 (1995).

[31] I. Yamaguchi, and T. Zhang, "Phase-shifting digital holography," Opt. Lett. **22**, 1268-1270 (1997).

[32] M. Takeda, H. Ina, and S. Kobayashi, "Fourier-transform method of fringe-pattern analysis for computer-based topography and interferometry," J. Opt. Soc. Am. **72**, 156-160 (1982).

[33] C. Froehly, A. Lacourt, and J. C. Vienot, "Time Impulse Responce and time Frequency Responce of Optical Pupils," Nouvelle Revue D'Optique **4**, 183-196 (1973).

[34] C. Iaconis, and I. A. Walmsley, "Spectral phase interferometry for direct electric-field reconstruction of ultrashort optical pulses," Opt. Lett. **23**, 792-794 (1998).

[35] J. A. Squier, and M. Müller, "High resolution non linear microscopy: A review of sources and methods for achieving optical imaging," Rev. Sci. Instrum. **72**, 2855-2867 (2001).

[36] M. Young, *Optics and Lasers* (Springer, 2000).

[37] J. Y. Wang, and D. E. Silva, "Wave-front interpretation with Zernike polynomials," Appl. Opt. **19**, 1510-1518 (1980).

[38] R. K. Tyson, "Conversion of Zernike aberration coefficients to Seidel and higher-order power-series aberration coefficients," Opt. Lett. **7**, 262-264 (1982).

[39] G. Conforti, "Zernike aberration coefficients from Seidel and higher-order power-series coefficients," Opt. Lett. **8**, 407-408 (1983).

[40] M. Kempe, and W. Rudolph, "Femtosecond pulses in the focal region of lenses," Phys. Rev. A **48**, 4721-4729 (1993).

[41] M. Kempe, and W. Rudolph, "Impact of chromatic and spherical aberration on the focusing of ultrashort light pulses by lenses," Opt. Lett. **18**, 137-139 (1993).

[42] Z. Bor, "Distortion of femtosecond laser pulses in lenses," Opt. Lett. **14**, 119-121 (1989).

[43] J. B. Guild, C. Xu, and W. W. Webb, "Measurement of group delay dispersion of high numerical aperture objective lenses using two-photo excited fluorescence," Appl. Opt. **36**, 397-401 (1997).

[44] M. Müller, J. A. Squier, and G. J. Brakenhoff, "Measurement of femtosecond pulses in the focal point of high-numerical-aperture lens by two-photon absorption," Opt. Lett. **20**, 1038-1040 (1995).

[45] T. A. Planchon, S. Ferré, G. Hamoniaux, G. Chériaux, and J.-P. Chambaret, "Experimental evidence of 25-fs laser pulse distortion in singlet beam expanders," Opt. Lett. **29**, 2300-2302 (2004).

[46] J. Jasapara, and W. Rudolph, "Characterization of sub-10-fs pulse focusing with high-numerical-aperture microscope objectives," Opt. Lett. **24**, 777-779 (1999).

[47] D. N. Fittinghoff, A. C. Millard, J. A. Squier, and M. Müller, "Frequency-Resolved Optical Gating Measurement of Ultrashort Pulses Passing Through a High Numerical Aperture Objective," IEEE J. Quantum Electron. **35**, 479-486 (1999).

[48] L. Cohen, *Time-frequency analysis* (Prentice Hall, 1995).

[49] R. Netz, T. Feurer, R. Wolleschensky, and R. Sauerbrey, "Measurement of the pulse-front distortion in high-numerical-aperture optics," Applied Physics B (Lasers and Optics) **70**, 833-837 (2000).

[50] E. M. Kosik, A. S. Radunsky, I. A. Walmsley, and C. Dorrer, "Interferometric technique for measuring broadband ultrashort pulses at the sampling limit," Opt. Lett. **30**, 326-328 (2005).

[51] K. Osvay, A. P. Kovács, Z. Heiner, G. Kurdi, J. Klebniczki, and M. Csatári, "Angular Dispersion and Temporal Change of Femtosecond Pulses From

Misaligned Pulse Compressors," IEEE J. Sel. Top. Quant. Electron. **10**, 213-220 (2004).

[52] P. Gabolde, and R. Trebino, "Self-referenced measurement of the complete electric field of ultrashort pulses," Opt. Express **12**, 4423-4428 (2004).

[53] D. Gabor, "Microscopy by reconstructed wave-fronts," Proceedings of the Royal Society of London A **197**, 454-487 (1949).

[54] P. Hariharan, *Optical Holography. Principles, techniques, and applications* (University of Cambridge, 1996).

[55] U. Schnars, and W. Jüptner, "Direct recording of holograms by a CCD target and numerical reconstruction," Appl. Opt. **33**, 179-181 (1994).

[56] E. N. Leith, and J. Upatnieks, "Reconstructed Wavefronts and Communication Theory," J. Opt. Soc. Am. **52**, 1123-1130 (1962).

[57] C. W. Chen, and H. A. Zebker, "Two-dimensional phase unwrapping with use of statistical models for cost functions in nonlinear optimization," J. Opt. Soc. Am. A **18**, 338-351 (2001).

[58] S. Lai, B. King, and M. A. Neifeld, "Wave front reconstruction by means of phase-shifting digital in-line holography," Opt. Commun. **173**, 155-160 (2000).

[59] I. Yamaguchi, J.-i. Kato, S. Ohta, and J. Mizuno, "Image formation in phase-shifting digital holography and applications to microscopy," Appl. Opt. **40**, 6177-6186 (2001).

[60] J.-i. Kato, I. Yamaguchi, and T. Matsumura, "Multicolor digital holography with an achromatic phase shifter," Opt. Lett. **27**, 1403-1405 (2002).

[61] S. Grilli, P. Ferraro, S. De Nicola, A. Finizo, G. Pierattini, and R. Meucci, "Whole optical wavefields reconstruction by Digital Holography," Opt. Express **9**, 294-302 (2001).

[62] W. Xu, M. H. Jericho, I. A. Meinertzhagen, and H. J. Kreuzer, "Digital in-line holography for biological applications," Proc. Natl. Acad. Sci. U. S. A. **98**, 11301-11305 (2001).

[63] M. Born, and E. Wolf, *Principles of Optics* (University Press, Cambridge, 1999).

[64] M. Centurion, Y. Pu, Z. Liu, D. Psaltis, and T. W. Hansch, "Holographic recording of laser-induced plasma," Opt. Lett. **29**, 772-774 (2003).

[65] Z. Bor, Z. Gogolak, and G. Szabo, "Femtosecond-resolution pulse-front distortion measurement by time-of-flight interferometry," Opt. Lett. **14**, 862-864 (1989).

[66] L. Yu, and M. K. Kim, "Wavelength-scanning digital interference holography for tomographic three-dimensional imaging by use of the angular spectrum method," Opt. Lett. **30**, 2092-2094 (2005).

[67] E. Arons, D. Dilworth, M. Shih, and P. C. Sun, "Use of Fourier synthesis holography to image through inhomogeneities," Opt. Lett. **18**, 1852-1854 (1993).

[68] T. Colomb, P. Dahlgren, D. Beghuin, E. Cuche, P. Marquet, and C. Depeursinge, "Polarization imaging by use of digital holography," Appl. Opt. **41**, 27-37 (2002).

[69] J. P. Geindre, P. Audebert, A. Rousse, F. Falliès, J. C. Gauthier, A. Mysyrowicz, A. Dos Santos, G. Hamoniaux, and A. Antonetti, "Frequency-domain interferometer for measuring the phase and amplitude of a femtosecond pulse probing a laser-produced plasma," Optics Letters **19**, 1997-1999 (1997).

[70] T. Tanabe, H. Tanabe, Y. Teramura, and F. Kannari, "Spatiotemporal measurements based on spatial spectral interferometry for ultrashort optical pulses shaped by a Fourier pulse shaper," J. Opt. Soc. Am. B **19**, 2795-2802 (2002).

[71] C. Dorrer, and I. A. Walmsley, "Simple linear technique for the measurement of space-time coupling in ultrashort optical pulses," Opt. Lett. **27**, (2002).

[72] C. Dorrer, E. M. Kosik, and I. A. Walmsley, "Spatio-temporal characterization of the electric field of ultrashort pulses using two-dimensional shearing interferometry," Applied Physics B (Lasers and Optics) **74 [Suppl.]**, S209-S217 (2002).

[73] L. Gallmann, G. Steinmeyer, D. H. Sutter, T. Rupp, C. Iaconis, I. A. Walmsley, and U. Keller, "Spatially resolved amplitude and phase characterization of femtosecond optical pulses," Opt. Lett. **26**, 96-98 (2001).

[74] S. A. Diddams, H. K. Eaton, A. A. Zozulya, and T. S. Clement, "Full-field characterization of femtosecond pulses after nonlinear propagation," Conference on Lasers and Electro-Optics, Paper CFF3 (1998).

[75] P. Almoro, M. Cadatal, W. Garcia, and C. Saloma, "Pulsed full-color digital holography with a hydrogen Raman shifter," Appl. Opt. **43**, 2267-2271 (2004).

[76] I. Yamaguchi, T. Matsumura, and J.-i. Kato, "Phase-shifting color digital holography," Opt. Lett. **27**, 1108-1110 (2002).

[77] Z. Liu, M. Centurion, G. Panotopoulos, J. Hong, and D. Psaltis, "Holographic recording of fast events on a CCD camera," Opt. Lett. **27**, 22-24 (2002).

[78] E. Leith, C. Chen, Y. Chen, D. Dilworth, J. Lopez, J. Rudd, P. C. Sun, J. Valdmanis, and G. Vossler, "Imaging through scattering media with holography," J. Opt. Soc. Am. A **9**, 1148-1153 (1992).

[79] S. Rivet, L. Canioni, R. Barille, and L. Sarger, "Multidimensional Shearing for Linear and Nonlinear Propagation Analysis.," Ultrafast Optics Conference, Paper M20 (2001).

[80] P. O'Shea, M. Kimmel, X. Gu, and R. Trebino, "Highly simplified device for ultra-short measurement," Opt. Lett. **26**, 932-934 (2001).

[81] M. Bass, "Handbook of Optics, 2nd ed.," 42.89-42.90 (1995).

[82] P. H. Lissberger, and W. L. Wilcock, "Properties of All-Dielectric Interference Filters. II. Filters in Parallel Beams of Light Incident Obliquely and in Convergent Beams," J. Opt. Soc. Am. **29**, 126-130 (1959).

[83] D. Malacara, *Optical Shop Testing* (John Wiley & Sons, 1992).

[84] J. Liang, B. Grimm, S. Goelz, and J. F. Bille, "Objective measurement of wave aberrations of the human eye with the use of a Hartmann-Shack sensor," J. Opt. Soc. Am. A **11**, 1949-1957 (1994).

[85] J. A. Buck, *Fundamentals of Optical Fibers* (Wiley, 2004).

[86] R. Paschotta, R. Häring, E. Gini, H. Melchior, U. Keller, H. L. Offerhaus, and D. J. Richardson, "Passively Q-switched 0.1-mJ fiber laser system at 1.53 um," Opt. Lett. **24**, 388-390 (1999).

[87] L. R. Brovelli, U. Keller, and T. H. Chiu, "Design and operation of antiresonant Fabry-Perot saturable semiconductor absorbers for mode-locked solid-state lasers," J. Opt. Soc. Am. B **12**, 311-322 (1995).

[88] P. F. Van Kessel, L. J. Hornbeck, R. E. Meier, and M. R. Douglass, "A MEMS-Based Projection Display," Proc. IEEE **86**, 1687-1704 (1998).

[89] S. Akturk, M. Kimmel, and R. Trebino, "Extremely simple device for measuring 1.5-um ultrashort laser pulses," Opt. Express **12**, 4483-4489 (2004).

[90] P. Gabolde, and R. Trebino, "Single-shot measurement of the full spatio-temporal field of ultrashort pulses with multi-spectral digital holography," Opt. Express **14**, 11460-11467 (2006).

[91] C. Dorrer, E. M. Kosik, and I. A. Walmsley, "Direct space-time characterization of the electric fields of ultrashort optical pulses," Opt. Lett. **27**, 548-550 (2002).

[92] E. Hecht, *Optics* (Addison-Wesley, 1998).

[93] P. H. Lissberger, "Properties of All-Dielectric Interference Filters. I. A New Method of Calculation," J. Opt. Soc. Am. **49**, 121-125 (1959).

[94] J. P. Uyemura, *Introduction to VLSI Circuits and Systems* (Wiley, 2001).

[95] P. O'Shea, S. Akturk, M. Kimmel, and R. Trebino, "Practical issues in ultra-short-pulse measurements with 'GRENOUILLE'," Applied Physics B (Lasers and Optics) **79**, 683-691 (2004).

[96] K. Naganuma, K. Mogi, and H. Yamada, "Group-delay measurement using the Fourier transform of an interferometric cross correlation generated by white light," Opt. Lett. **15**, 393-395 (1990).

[97] A. Brodeur, and S. L. Chin, "Ultrafast white-light continuum generation and self-focusing in transparent condensed media," J. Opt. Soc. Am. B **16**, 637-649 (1999).

[98] C. Bhan, L. Mainali, D. Mohan, and A. K. Gupta, "Recycling of undiffracted laser light for reconstruction of holograms," Optics and Lasers in Engineering **35**, 355-360 (2001).

[99] P. Gabolde, D. Lee, S. Akturk, and R. Trebino, "Describing first-order spatio-temporal distortions in ultrashort pulses using normalized parameters," Opt. Express **15**, 242-251 (2007).

[100] R. L. Fork, O. E. Martinez, and J. P. Gordon, "Negative dispersion using pairs of prisms," Opt. Lett. **9**, 150-152 (1984).

[101] S. Akturk, M. Kimmel, P. O'Shea, and R. Trebino, "Measuring pulse-front tilt in ultrashort pulses using GRENOUILLE," Opt. Express **11**, 491-501 (2003).

[102] K. Varju, A. P. Kovacs, G. Kurdi, and K. Osvay, "High-precision measurement of angular dispersion in a CPA laser," Appl. Phys. B **Suppl.**, 259-263 (2002).

[103] M. Kempe, U. Stamm, B. Wilhelmi, and W. Rudolph, "Spatial and temporal transformation of femtosecond laser pulses by lenses and lens systems," J. Opt. Soc. Am. B **9**, 1158-1165 (1992).

[104] X. Gu, S. Akturk, and R. Trebino, "Spatial chirp in ultrafast optics," Opt. Commun. **242**, 599-604 (2004).

[105] A. G. Kostenbauder, "Ray-Pulse Matrices: A Rational Treatment for Dispersive Optical Systems," IEEE J. Quantum Electron. **26**, 1148-1157 (1990).

[106] R. V. Hogg, and A. Craig, *Introduction to Mathematical Statistics* (Prentice Hall, 1994).

[107] Z. Bor, and B. Racz, "Group velocity dispersion in prisms and its application to pulse compression and travelling-wave excitation," Opt. Commun. **54**, 165-170 (1985).

[108] S. Akturk, X. Gu, E. Zeek, and R. Trebino, "Pulse-front tilt caused by spatial and temporal chirp," Opt. Express **12**, 4399-4410 (2004).

[109] K. Kato, "Second-Harmonic Generation to 2048 A in b-BaB2O4," IEEE J. Quantum Electron. **22**, 1013-1014 (1986).

[110] G. Rousseau, N. McCarthy, and M. Piché, "Description of pulse propagation in a dispersive medium by use of a pulse quality factor," Opt. Lett. **27**, 1649-1651 (2002).

[111] J. Peatross, and A. Rundquist, "Temporal decorrelation of short laser pulses," J. Opt. Soc. Am. B **15**, 216-222 (1998).

[112] V. V. Lozovoy, I. Pastirk, and M. Dantus, "Multiphoton intrapulse interference. IV. Ultrashort laser pulse spectral phase characterization and compensation," Opt. Lett. **29**, 775-777 (2004).

[113] R. Trebino, and D. J. Kane, "Using phase retrieval to measure the intensity and phase of ultrashort pulses: Frequency-resolved optical gating," J. Opt. Soc. Am. A **10**, 1101-1111 (1993).

[114] J. Collier, C. Danson, C. Johnson, and C. Mistry, "Uniaxial single shot autocorrelator," Rev. Sci. Instrum. **70**, 1599-1602 (1999).